condensed matter

MDPI

Article

Systematic Trends in Hybrid-DFT Computations of $BaTiO_3/SrTiO_3$, $PbTiO_3/SrTiO_3$ and $PbZrO_3/SrZrO_3$ (001) Hetero Structures

Roberts I. Eglitis [1,*], Sergei Piskunov [1], Anatoli I. Popov [1], Juris Purans [1], Dmitry Bocharov [1,2] and Ran Jia [1,3]

[1] Institute of Solid State Physics, University of Latvia, 8 Kengaraga Str., LV1063 Riga, Latvia
[2] Transport and Telecommunication Institute, Lomonosov Str. 1, LV1019 Riga, Latvia
[3] Laboratory of Theoretical and Computational Chemistry, Institute of Theoretical Chemistry, Jilin University, Changchun 130023, China
* Correspondence: rieglitis@gmail.com; Tel.: +371-26426703

Abstract: We performed predictive hybrid-DFT computations for $PbTiO_3$, $BaTiO_3$, $SrTiO_3$, $PbZrO_3$ and $SrZrO_3$ (001) surfaces, as well as their $BaTiO_3/SrTiO_3$, $PbTiO_3/SrTiO_3$ and $PbZrO_3/SrZrO_3$ (001) heterostructures. According to our hybrid-DFT computations for BO_2 and AO-terminated ABO_3 solid (001) surfaces, in most cases, the upper layer ions relax inwards, whereas the second layer ions shift upwards. Our hybrid-DFT computed surface rumpling *s* for the BO_2-terminated ABO_3 perovskite (001) surfaces almost always is positive and is in a fair agreement with the available LEED and RHEED experiments. Computed B-O atom chemical bond population values in the ABO_3 perovskite bulk are enhanced on its BO_2-terminated (001) surfaces. Computed surface energies for BO_2 and AO-terminated ABO_3 perovskite (001) surfaces are comparable; thus, both (001) surface terminations may co-exist. Our computed ABO_3 perovskite bulk Γ-Γ band gaps are in fair agreement with available experimental data. BO_2 and AO-terminated (001) surface Γ-Γ band gaps are always reduced with regard to the respective bulk band gaps. For our computed BTO/STO and PTO/STO (001) interfaces, the average augmented upper-layer atom relaxation magnitudes increased by the number of augmented BTO or PTO (001) layers and always were stronger for TiO_2-terminated than for BaO or PbO-terminated upper layers. Our B3PW concluded that BTO/STO, as well as SZO/PZO (001) interface Γ-Γ band gaps, very strongly depends on the upper augmented layer BO_2 or AO-termination but considerably less so on the number of augmented (001) layers.

Keywords: ABO_3 perovskites; (001)interfaces; $BaTiO_3/SrTiO_3$; $PbTiO_3/SrTiO_3$; $SrZrO_3/PbZrO_3$

Citation: Eglitis, R.I.; Piskunov, S.; Popov, A.I.; Purans, J.; Bocharov, D.; Jia, R. Systematic Trends in Hybrid-DFT Computations of $BaTiO_3/SrTiO_3$, $PbTiO_3/SrTiO_3$ and $PbZrO_3/SrZrO_3$ (001) Hetero Structures. *Condens. Matter* **2022**, *7*, 70. https://doi.org/10.3390/condmat7040070

Academic Editor: Antonio Bianconi

Received: 1 November 2022
Accepted: 25 November 2022
Published: 29 November 2022

1. Introduction

Different aspects of (001) surface as well as (001) interface phenomena in ABO_3 perovskites are topics of paramount importance in modern solid state physics [1–16]. All of our hybrid-DFT computed $SrZrO_3$, $PbZrO_3$, $PbTiO_3$, $BaTiO_3$ and $SrTiO_3$ solids belong to the group of so-called ABO_3 perovskite compounds [17–19]. Strontium zirconate ($SrZrO_3$) is an extremely interesting material due to its high-temperature electronic properties [20]. The $SrZrO_3$ phase transitions have been very carefully examined by Kennedy et al. [21] by means of powder neutron diffraction, as well as the Rietveld method [21]. Maniwa et al. [22] and Shirane et al. [23] described $PbZrO_3$ as antiferroelectric due to its dielectric behaviour. Since then, materials that revealed a structural phase transition between two non-polar phases with a large dielectric anomaly at the high-temperature region of the transition were called antiferroelectrics [22,23]. Antiferroelectric oxides, for example $PbZrO_3$, become highly promising candidate materials for dielectric energy storage capacitors [24,25]. $PbTiO_3$ is a crucial component in a wide range of industrially important applications, including sensors, ultrasonic transducers and actuators [26]. Polymer

ceramic hybrid composites (PVA/$PbTiO_3$) are highly promising functional materials in a wide variety of research disciplines, demonstrating useful electrical, optical, mechanical, thermal and antibacterial properties [27]. Ferroelectric materials, for example $BaTiO_3$, have been mentioned in connection to bacterial degradation [28]. It is demonstrated that the remnant polarization can induce antibacterial activities [29] in ferroelectric materials like $BaTiO_3$. Lead zirconate titanate $Pb(Zr,Ti)O_3$ is the most widely used worldwide piezoceramic material for electromechanical device applications [30]. Strontium titanate exhibits photocatalytic activity [31,32]. The identification of highly promising thermoelectric materials, like $SrTiO_3$, is accelerated by theoretical predictions from ab initio calculations [33–36]. In general, there is a lot of interest in the science and technology of transition metal oxides, like ABO_3 perovskites, due to their large variety of specific electronic, optical and magnetic properties [37–48]. For that reason, during the last 25 years, a lot of theoretical and experimental studies have been performed for $PbTiO_3$, $BaTiO_3$, $SrTiO_3$, $SrZrO_3$ and $PbZrO_3$ perovskite (001) surfaces [49–72]. At the same time, it is very difficult to understand why a smaller number of first-principles computations, as well as experimental studies, were devoted to BTO/STO and PTO/STO, as well as SZO/PZO (001) heterostructures [73–88].

$SrTiO_3$ (STO) perovskite is paraelectric and maintains its cubic centrosymmetric structure at all observed temperatures [89]. $BaTiO_3$ (BTO), as a function of temperature, undergoes three phase transitions. Namely, the BTO crystal structure changes at 183 K from rhombohedral (*R*3m) to orthorhombic (*A*mm2), then at 278 K to tetragonal (*P*4mm), and finally at 403 K to a high-temperature cubic structure ($Pm\bar{3}m$) [90]. $PbTiO_3$ (PTO) undergoes only one phase transition at 766 K from a tetragonal ferroelectric phase, stable at room temperature, with the space group *P*4mm to the high-symmetry cubic structure with the space group $Pm\bar{3}m$ [91]. It is well-known that the classical $PbZrO_3$ (PZO) perovskite exhibits three different phases. Namely, at low temperatures, PZO has an orthorhombic antiferroelectric phase stable at the temperature region up to 230 °C. The PZO rhombohedral ferroelectric phase is stable at the temperature region from 230 °C to 233 °C. Finally, PZO perovskite possesses a cubic paraelectric phase at temperatures above 233 °C [69]. Lastly, for the $SrZrO_3$ (SZO) perovskite, Ligny et al. [92] discovered the following three phase transitions from enthalphy measurements: orthorhombic (*P*nma) → orthorhombic (*C*mcm) → tetragonal ($I4/mcm$) → cubic ($Pm\bar{3}m$) at temperatures equal to 995 K and 1105 K, as well as 1140 K, respectively [92].

For our hybrid-DFT computations, we adopted the classical cubic unit cells of $SrZrO_3$, $PbZrO_3$, $PbTiO_3$, $BaTiO_3$ and $SrTiO_3$ perovskites. The cubic unit cells of all five of our ab initio computed ABO_3 perovskites contain five atoms [93–96]. They all have exactly the same space group $Pm\bar{3}m$, as well as the same space group number, 221. In the cubic ABO_3 perovskite matrix, the A-type atom (Sr, Pb or Ba) was located at the cube corner position. Thereby, the ABO_3 perovskite A atom, in our computations, is located at the coordinate system origin and has the following coordinates (0, 0, 0). The B-type ABO_3 perovskite atom (Ti or Zr) is located at the body center location of the cube. The coordinates of the B atom are equal to ($\frac{1}{2}$, $\frac{1}{2}$, $\frac{1}{2}$). Finally, the ABO_3 perovskite unit cell's three oxygen atoms are located at the cube face center positions with the following coordinates ($\frac{1}{2}$, $\frac{1}{2}$, 0), ($\frac{1}{2}$, 0, $\frac{1}{2}$), (0, $\frac{1}{2}$, $\frac{1}{2}$).

The aim of our research reported herein was to perform necessary additional hybrid-DFT computations for $SrZrO_3$, $PbZrO_3$, $PbTiO_3$, $BaTiO_3$ and $SrTiO_3$ perovskite (001) surfaces, as well as their (001) heterostructures, in order to complete our many years of lasting work in this direction, and to create a theory that explains systematic trends in ABO_3 perovskite (001) surface and interface computations. In the first part of our contribution, we present comparative hybrid-DFT computation results dealing with the pristine $SrZrO_3$, $PbZrO_3$, $PbTiO_3$, $BaTiO_3$ and $SrTiO_3$ (001) surfaces. We computed the $SrZrO_3$, $PbZrO_3$, $PbTiO_3$, $BaTiO_3$ and $SrTiO_3$ (001) surface atom relaxations for both possible BO_2 and AO (001) surface terminations and compared the calculated surface rumplings *s* and interlayer distances Δd_{ij} with the available experimental data. As a next step, we computed the $SrZrO_3$, $PbZrO_3$, $PbTiO_3$, $BaTiO_3$ and $SrTiO_3$ (001) surface energies, as well as B-O chemical band populations near the BO_2-terminated (001) surfaces. Finally, we

computed the band gaps for bulk $PbTiO_3$, $BaTiO_3$ and $SrTiO_3$ and their (001) surfaces by means of different exchange-correlation functionals. As a logical next step, we extended our (001) surface calculations to hybrid-DFT computations of considerably less-studied $SrTiO_3/BaTiO_3$, $SrZrO_3/PbZrO_3$ and $PbTiO_3/SrTiO_3$ (001) heterostructures.

The present paper is structured in the following way. Our hybrid-DFT calculations details, dealing with ABO_3 perovskite (001) surfaces and heterostructures, are described in Section 2. Section 3.1 presents our computation results dealing with $SrZrO_3$, $PbZrO_3$, $PbTiO_3$, $BaTiO_3$ and $SrTiO_3$ (001) surfaces, whereas Section 3.2 addresses their $SrTiO_3/BaTiO_3$, $SrZrO_3/PbZrO_3$ and $PbTiO_3/SrTiO_3$ (001) heterostructures. In particular, our novel hybrid-DFT computations are devoted to charge density redistribution and changes in the band structure in stoichiometric, as well as non-stoichiometric (001), heterostructures, consisting of BTO, PTO and PZO (001) thin films, with different thicknesses deposited on the TiO_2-, TiO_2- and ZrO_2-terminated STO and SZO (001) substrate. We analyzed our hybrid-DFT calculation results and detected systematic trends common for all STO/BTO and STO/PTO, as well as SZO/PZO (001), heterostructures.

2. Hybrid-DFT Calculation Details

We carried out our hybrid-DFT computations for the $PbTiO_3$ (PTO), $BaTiO_3$ (BTO), $SrTiO_3$ (STO), $PbZrO_3$ (PZO) and $SrZrO_3$ (001) bulk, as well as their BO_2- and AO-terminated (001) surfaces, and their different (001) heterostructures, employing the computer code CRYSTAL [97]. For our hybrid-DFT computations, we employed the nowadays very popular hybrid exchange-correlation functionals B3LYP [98] or B3PW [99,100]. It is worthwhile to note that the hybrid exchange-correlation functionals, for example, B3LYP or B3PW allows achieving an outstanding agreement with the experiment for the band gaps of ABO_3 perovskites as well as related materials, like CaF_2 [101] and MgF_2 [102]. In contrast, density functional theory (DFT) strongly underestimates, while the Hartree–Fock (HF) method, as a rule, very strongly overestimates the ab initio calculated band gaps of solids. For example, the experimental CaF_2 direct band gap value at the Γ-point is equal to 12.1 eV [103]. Our, by means of Perdew–Burke–Ernzerhof (PBE) exchange-correlation functional [104,105], extensively used in DFT, ab initio computed CaF_2 Γ-Γ band gap is very strongly underestimated with respect to the experimental value (12.1 eV) and is equal to 8.45 eV. From another side, our ab initio HF [106] computed CaF_2 Γ-Γ band gap (20.77 eV) is 1.72 times overestimated compared to the experimental CaF_2 band gap value (12.1 eV [105]). According to our hybrid-DFT computations, the hybrid exchange correlation functionals, like B3LYP (10.85 eV) and B3PW (10.96 eV) allows the achievement of the best possible agreement with the experimental CaF_2 Γ-Γ band gap equal to 12.1 eV. The experimentally measured MgF_2 Γ-Γ band gap is equal to 13.0 eV [107]. Again, our PBE exchange-correlation functional computed MgF_2 Γ-Γ band gap is considerably underestimated regarding the experimental value of (13.0 eV) and is equal to 6.9 eV. In contrast, our ab initio HF computed MgF_2 Γ-Γ band gap (19.65 eV) very strongly, namely 1.65 times, overestimates the experimentally measured MgF_2 band gap at Γ-point (13.0 eV). The best possible results, according to our hybrid-DFT computations, are possible to achieve by means of the hybrid exchange-correlation functionals B3LYP (9.42 eV) and B3PW (9.48 eV). Since, as it is possible to see from our computation results for CaF_2 and MgF_2 solids, the hybrid exchange-correlation functionals B3LYP and B3PW allows achieving the best possible results for CaF_2 and MgF_2 Γ-Γ band gaps, we performed all of our coming ABO_3 perovskite (001) surface and interface computations using the B3LYP or B3PW functionals. The B3LYP and B3PW hybrid exchange-correlation functionals make use of 20% of the Hartree–Fock method as well as 80% of the density functional Hamiltonian, when incorporated in the CRYSTAL computer code [97].

The major advantage of the CRYSTAL computer software package, which is of key importance for our hybrid-DFT computations of neutral $SrZrO_3$, $PbZrO_3$, $PbTiO_3$, $BaTiO_3$ and $SrTiO_3$ (001) surfaces and interfaces, is the implementation of the isolated 2-dimensional (2D) slab model. In our hybrid-DFT computations, the reciprocal space integration was

carried out by examining the Brillouin zone with the 8 × 8 × 8 times expanded Pack–Monkhorst net for the bulk of $SrZrO_3$, $PbZrO_3$, $PbTiO_3$, $BaTiO_3$ and $SrTiO_3$ solids, as well as by 8 × 8 × 1 net for their (001) surfaces and interfaces. With a goal of reaching a high accuracy in our ab initio computations, we employed sufficiently large tolerances equal to 7, 8, 7, 7, 14 for the Coulomb overlap, Coulomb penetration and exchange overlap, as well as first exchange pseudo-overlap and the second exchange pseudo-overlap [97].

With the aim of computing the neutral BO_2-terminated (001) surfaces of ABO_3 solids, we customized symmetrical slabs. They involved nine neutral as well as alternating BO_2 and AO layers (Figure 1). All of these nine layers were perpendicular to the [001] crystal direction [108–111]. Taking into consideration the standard ionic charges equal to (+2*e*) for the A atom and (+4*e*) for the B atom, as well as (−2*e*) for the O atom, both alternating BO_2 and AO layers are neutral, since they have a summary slab charge equal to zero. The slab, containing nine layers, used by us for the BO_2-terminated ABO_3 perovskite (001) surface computations (Figure 1) consisted of a supercell containing 23 atoms. Our hybrid-DFT computed BO_2-terminated (001) slabs (Figure 1) of ABO_3 perovskite were non-stoichiometric. They have a unit cell, used in our hybrid-DFT computations, described by the following chemical formula—$A_4B_5O_{14}$ [112–114].

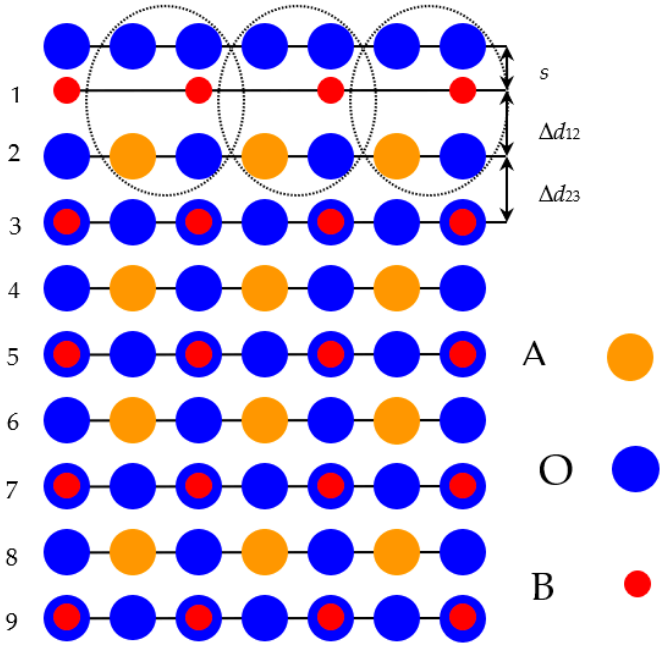

Figure 1. Profile for the BO_2-terminated (001) surface of ABO_3 perovskite containing nine layers. The definitions of surface rumpling *s* as well as the near-surface interplanar separations Δd_{12} and Δd_{23} are explained.

The second slab in our hybdid-DFT computations was terminated from both sides by the AO planes (Figure 2). It also contained nine alternating layers (Figure 2) but consisted of a supercell that incorporated only 22 atoms. Furthermore, the AO-terminated nine-layer slab, used in our hybrid-DFT computations, was non-stoichiometric and has the following chemical formula—$A_5B_4O_{13}$. For Sr, Ba, Pb, Ti and O atoms [115], we used the basis sets developed in [117]. The inner-core electrons for Sr, Ba, Pb, Ti and Zr atoms were described by a small core Hay–Wadt effective pseudopotentials [97,116]. We computed the number of light oxygen atoms using the all-electron basis sets [97,115]. In order to correctly define the chemical bonding in ABO_3 perovskites, as well as covalency effects, we employed a widely accepted Mulliken population [117–119] analysis. The Mulliken population analysis is incorporated in the CRYSTAL computer code [97], used in all of our hybrid-DFT computations for the ABO_3 solid (001) surfaces and their respective heterostructures (Figure 3).

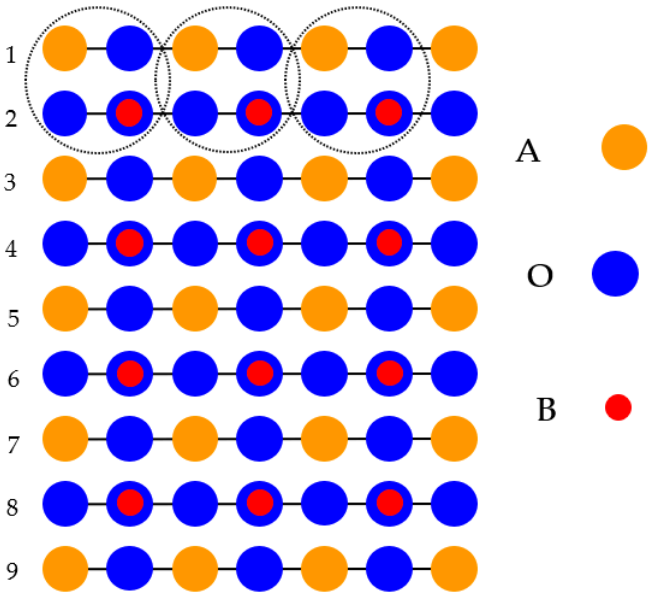

Figure 2. Profile for the AO-terminated (001) surface of ABO_3 perovskite containing nine layers.

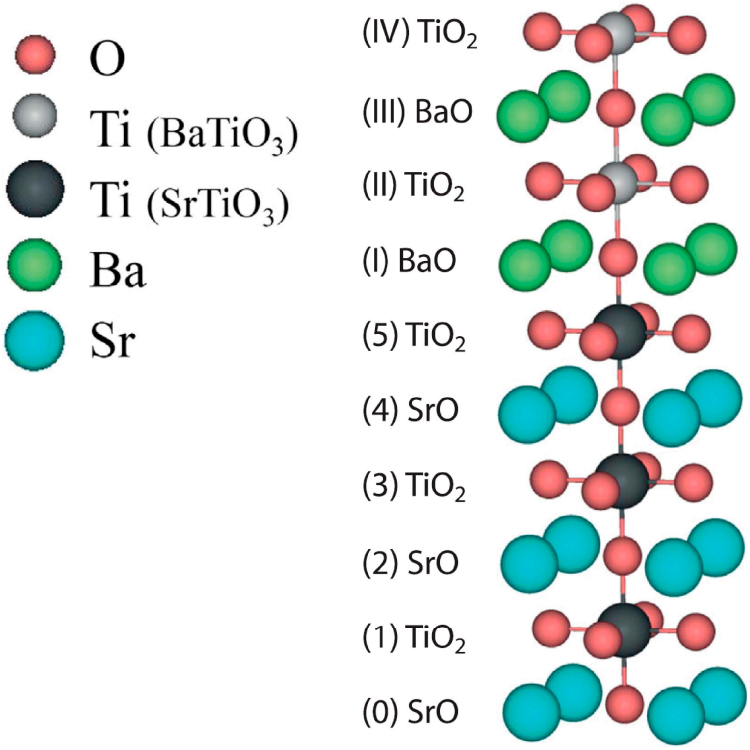

Figure 3. Profile of the (001) interface among the cubic perovskites $BaTiO_3$ and $SrTiO_3$. $SrTiO_3$ substrate planes are numbered using Arabic numbers. Planes of the augmented $BaTiO_3$ (001) film are numbered using Roman numbers. Number 0 denotes the central (SrO) plane of the symmetrically TiO_2-terminated 11-layer $SrTiO_3$ (001) substrate.

With ambition to compute the ABO_3 solid (001) surface energies, we opened our hybid-DFT computations with cleavage energies for unrelaxed AO- as well as BO_2-terminated (001) surfaces. In our hybrid-DFT computations, the two nine-layer AO- as well as BO_2-terminated slabs contained 22 and 23 atoms of each of them. These two AO- and BO_2-terminated slabs represented together nine ABO_3 perovskite bulk unit cells. Each ABO_3 perovskite bulk unit cell contained five atoms. AO as well as BO_2-terminated ABO_3 perovskite (001) surfaces arose at the same time moment under crystal cleavage. Therefore,

the relevant cleavage energy is shared uniformly among created surfaces. Thereby, our ab initio computed ABO_3 perovskite (001) surface cleavage energy is equal for both AO- as well as BO_2-terminations:

$$E_{surf}{}^{unrel} = ¼ [E_{slab}{}^{unrel} (AO) + E_{slab}{}^{unrel} (BO_2) - 9\ E_{bulk}] \quad (1)$$

where $E_{slab}{}^{unrel}$ (AO) and $E_{slab}{}^{unrel}$ (BO_2) are our hybrid-DFT computed total energies for unrelaxed AO- and BO_2-terminated ABO_3 perovskite nine-layer slabs. E_{bulk} is our hybrid-DFT computed total bulk unit cell energy containing five atoms. Factor 4 in Equation (1) arises from the fact that we created four surfaces during the ABO_3 perovskite cleavage event. As a next step, we computed the relaxation energies for AO- and BO_2-terminated ABO_3 solid (001) surfaces. We relaxed both sides of our nine-layer AO- and BO_2-terminated slabs.

$$E_{rel}(\Psi) = ½ [E_{slab} (\Psi) - E_{slab}{}^{unrel} (\Psi)] \quad (2)$$

$E_{slab}(\Psi)$ is our hybrid-DFT computed slab total energy after the geometry relaxation. In our case the symbol Ψ denotes AO- or BO_2-terminated ABO_3 perovskite (001) surface. After all of our hybrid-DFT computed ABO_3 perovskite AO- or BO_2-terminated (001) surface energy is defined as a sum of the cleavage as well as relaxation energies:

$$E_{surf}(\Psi) = E_{surf}{}^{unrel} + E_{rel}(\Psi) \quad (3)$$

As a next step, we will discuss our calculation details for the ABO_3 perovskite (001) heterostructures, using as an example the $BaTiO_3/SrTiO_3$ (001) interface. At room temperature, the $SrTiO_3$ substrate has a high-symmetry cubic structure. In our hybrid-DFT computations, we computed both $SrTiO_3$ and $BaTiO_3$ perovskites at their cubic, high-symmetry phase with the space group number $Pm\bar{3}m$. In our hybrid-DFT computations, we modelled the $BaTiO_3/SrTiO_3$ (001) interface employing the single-slab model. In order to maximally apply the advantages of symmetry, our slabs were symmetrically terminated. In our hybrid-DFT computations, the $SrTiO_3$ (001) substrate always contained 11 alternating SrO as well as TiO_2 layers. From 1 to 10 BaO and TiO_2 alternating layers were augmented on both sides of the 11-layer TiO_2-terminated $SrTiO_3$ (001) substrate (Figure 3).

We allowed all coordinated of atoms to relax in our hybrid-DFT computed $BaTiO_3/SrTiO_3$ (001) heterostructure. In our hybrid-DFT computations, due to restrictions imposed by the cubic symmetry of the system, atomic displacements are possible only along axis *z*. It is worthwhile to note that the mismatch equal to approximately 2.5 percent among $BaTiO_3$ and $SrTiO_3$ bulk lattice constants happens at the time of $BaTiO_3$ epitaxial growth. The joint equilibrium average lattice constant employed in all of our future hybrid-DFT computations for $BaTiO_3/SrTiO_3$ (001) interfaces is equal to 3.958 Å. The joint lattice constant for the $BaTiO_3/SrTiO_3$ (001) interface was hybrid-DFT computed by us for the thickest (001) interface, which consisted of the 11-layer $SrTiO_3$ substrate as well as, from both sides of this substrate, augmented 10 $BaTiO_3$ layers. In our hybrid-DFT calculations of the shift (Δz) for each layer of the $BaTiO_3/SrTiO_3$ (001) heterostructure, we take into consideration the shift of the previous atomic layer. Therefore, the reference z coordinate for each mono-layer *N* is described by the following equation:

$$z_N{}^{ref} = ½ [z_{N-1}{}^{Me} + z_{N-1}{}^{O}) \quad (4)$$

where, in Equation (4), $z_{N-1}{}^{Me}$ as well as $z_{N-1}{}^{O}$ defines the *z* coordinates for the cation and anion from the previous atomic monolayer.

3. Hybrid-DFT Computation Results

3.1. Pristine $SrTiO_3$, $BaTiO_3$, $PbTiO_3$, $SrZrO_3$ and $PbZrO_3$ (001) Surfaces

As an opening to our hybrid-DFT computations, we computed the bulk lattice constants for five ABO_3 perovskites. Our hybrid-DFT computed bulk lattice constants for $PbTiO_3$ (3.936 Å), $BaTiO_3$ (4.008 Å), $SrTiO_3$ (3.904 Å), $PbZrO_3$ (4.220 Å) and $SrZrO_3$ (4.195 Å)

are in fair agreement with the experimentally detected bulk lattice constants for $PbTiO_3$ (3.97 Å [120]), $BaTiO_3$ (4.004 Å [121]), $SrTiO_3$ (3.898 Å [122]), $PbZrO_3$ (4.1614 Å [123]) and $SrZrO_3$ (4.154 Å [21]). Our hybrid-DFT computed effective atomic charges, as well as chemical bond populations for the $PbTiO_3$, $BaTiO_3$, $SrTiO_3$, $PbZrO_3$ and $SrZrO_3$ perovskite bulk, are collected in Table 1.

Table 1. Our hybrid-DFT computed effective atomic charges Q (in e) as well as bond populations P (in e) for atoms in $PbTiO_3$, $BaTiO_3$, $SrTiO_3$, $PbZrO_3$ and $SrZrO_3$ bulk matrices.

Bulk Properties		**$PbTiO_3$**	**$BaTiO_3$**	**$SrTiO_3$**	**$PbZrO_3$**	**$SrZrO_3$**
Ion	Property	B3PW	B3PW	B3PW	B3LYP	B3LYP
A	Q	+1.354	+1.797	+1.871	+1.368	+1.880
	P	+0.016	−0.034	−0.010	+0.030	+0.002
O	Q	−1.232	−1.388	−1.407	−1.160	−1.351
	P	+0.098	+0.098	+0.088	+0.106	+0.092
B	Q	+2.341	+2.367	+2.351	+2.111	+2.174

As we can see from Table 1, our hybrid-DFT computed atomic charges for all five perovskites are considerably smaller than those expected in an ionic model for the A atom (+2e), for the B atom (+4e) and also for the O atom (−2e). For example, our hybrid-DFT computed effective atomic charges for the Pb atom, in the different compounds $PbTiO_3$ (+1.354e) and $PbZrO_3$ (+1.368e), are almost equal. The same is also true for the Sr atom. Furthermore, the Sr atom atomic charges in different perovskites, such as $SrTiO_3$ (+1.871e) and $SrZrO_3$ (+1.880e), are almost equal (Table 1). The Zr atom effective charges in the $PbZrO_3$ (+2.111e) and $SrZrO_3$ (+2.174e) perovskites are almost equal and are always considerably smaller than the Ti atom effective charges in the $PbTiO_3$ (+2.341e), $BaTiO_3$ (+2.367e) and $SrTiO_3$ (+2.351e) crystals. It is worthwhile to note that the Ti atom effective charges in $PbTiO_3$, $BaTiO_3$ and $SrTiO_3$ perovskites (+2.341e, +2.367e and +2.351e, respectively) almost coincide (Table 1). The chemical bond covalency between the B and O atoms are in the range from (+0.088e) between Ti-O atoms in the $SrTiO_3$ perovskite to (+0.106e) between Zr-O atoms in the $PbZrO_3$ crystal. The bond populations between Ti-O atoms are equal to (0.098e) in both $PbTiO_3$ and $BaTiO_3$ perovskites.

As a next step, we computed the bulk band gaps at the Γ-point for $PbTiO_3$, $BaTiO_3$ and $SrTiO_3$ perovskites and plotted the band structure for $BaTiO_3$ and $PbTiO_3$ crystals. We compared our hybrid-DFT computation results for Γ-Γ band gaps with available experimental results. Our B3PW computed $SrTiO_3$ bulk Γ-Γ band gap is equal to 3.96 eV, which is in fair agreement with the available experimental data for $SrTiO_3$ direct Γ-Γ bulk band gap equal to 3.75 eV [124] (Table 2). The direct Γ-Γ bulk band gap in the $BaTiO_3$ perovskite is measured experimentally (Table 2) at the tetragonal to orthorhombic phase transition temperature equal to 278 K. The $BaTiO_3$ direct bulk Γ-Γ band gap in different experimental conditions is slightly different and is equal to 3.27 eV or 3.38 eV, respectively [125]. Our B3PW computed $BaTiO_3$ direct bulk Γ-Γ band gap (3.55 eV) (Table 2) is in almost perfect agreement with these experiments (Figure 4a). Finally, our B3PW computed $PbTiO_3$ bulk band gap at Γ-point (4.32 eV) (Figure 4b) (Table 2) is in satisfactory agreement with the experimentally detected direct $PbTiO_3$ bulk Γ-Γ band gap (3.4 eV) [126] at the $PbTiO_3$ perovskite tetragonal phase.

As we can see from Table 3, according to our hybrid-DFT computations, all upper-layer atoms for all five perovskites relax inwards in the direction towards the perovskite bulk. The only exception from this systematic trend is the upward relaxation of the TiO_2-terminated $PbTiO_3$ (001) surface upper-layer O atom by 0.31 % of a_0. Just opposite, all second-layer atoms relax upwards. For both upper layers, the metal atom relaxation magnitudes are always larger than the respective oxygen atom relaxation magnitude [127–130]. The only exception to this systematic trend is the ZrO_2-terminated $SrZrO_3$ (001) surface upper-layer oxygen atom relaxation magnitude (−2.10% of a_0), which is slightly larger than the same-layer Sr atom relaxation magnitude (−1.38% of a_0) (Table 3).

Table 2. Our B3PW computation results as well as the experimental data for $SrTiO_3$, $BaTiO_3$ and $PbTiO_3$ bulk Γ-Γ band gaps (in eV) and their structure at room temperature (RT).

Solid	Structure at RT	Exp. Γ-Γ Band Gap (eV)	Ab initio Γ-Γ Band Gap
$SrTiO_3$	Cubic phase	3.75 eV [124]	3.96 eV
$BaTiO_3$	Tetragonal ↔ orthorhombic phase at 278 K	3.38 eV (//c); 3.27 eV (⊥ c) [125]	3.55 eV
$PbTiO_3$	Tetragonal phase	3.4 eV [126]	4.32 eV

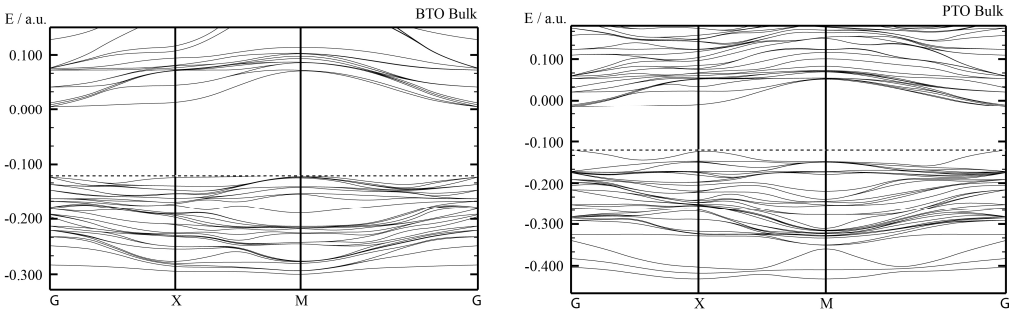

(**a**) (**b**)

Figure 4. Our B3PW computed electronic bulk band structure for $BaTiO_3$ (**a**) and $PbTiO_3$ (**b**) perovskites.

Table 3. Atomic relaxation magnitudes (in % of the a_0) for the BO_2-terminated $PbTiO_3$, $BaTiO_3$, $SrTiO_3$, $PbZrO_3$ and $SrZrO_3$ (001) surfaces.

Solid		$PbTiO_3$	$BaTiO_3$	$SrTiO_3$	$PbZrO_3$	$SrZrO_3$
Layer	Ion	TiO_2-t.	TiO_2-t.	TiO_2-t.	ZrO_2-t.	ZrO_2-t.
1	B	−2.81	−3.08	−2.25	−2.37	−1.38
	O	+0.31	−0.35	−0.13	−1.99	−2.10
2	A	+5.32	+2.51	+3.55	+4.36	+2.81
	O	+1.28	+0.38	+0.57	+1.04	+0.91
3	B	-	-	-	−0.47	−0.04
	O	-	-	-	−0.28	−0.05

In most cases, as it is possible to see from our hybrid-DFT computation results collected in Table 4 for AO-terminated $PbTiO_3$, $BaTiO_3$, $SrTiO_3$, $PbZrO_3$ and $SrZrO_3$ (001) surfaces, all upper-layer atoms relax inwards (Table 4), whereas all second-layer atoms relax upwards. The only two exceptions from this systematic trend are the upward relaxation of O atom on the upper layer of SrO-terminated $SrTiO_3$ (001) surface by (+0.84% of a_0), as well as the inward relaxation of the second-layer O atom on the SrO-terminated $SrZrO_3$ (001) surface by a very small relaxation magnitude of only (−0.05 of a_0) (Table 4). It is interesting to notice that for the AO-terminated $PbTiO_3$, $BaTiO_3$, $SrTiO_3$, $PbZrO_3$ and $SrZrO_3$ (001) surfaces, the relaxation magnitudes of metal atoms in the upper, as well as the second, surface layers are always larger than the relaxation magnitudes of the respective oxygen atoms (Table 4).

As we can see from Table 5, our hybrid-DFT computed surface rumpling s (Figure 1) is always positive for BO_2-terminated ABO_3 perovskite (001) surfaces. The definitions of surface rumpling s, as well as the near-surface interplanar separations Δd_{12} and Δd_{23}, are explained in Figure 1. The only exception to this systematic trend is our hybrid-DFT computed negative surface rumpling s for the ZrO_2-terminated $SrZrO_3$ (001) surface (−0.72) (Table 5). Moreover, the surface rumpling s computed by Wang et al. [131] for the ZrO_2-terminated $SrZrO_3$ (001) surface is negative (Table 5) (−0.70) and almost coincides with our result (−0.72). The experimental data for the surface rumpling s are available, for example, for the $SrTiO_3$ crystal. Our B3PW computed surface rumpling s for $SrTiO_3$

perovskite (+2.12) is in fair agreement with the available LEED [132] (+2.1 ± 2), as well as RHEED [133] (+2.6), experiments (Table 5). It is worthwhile to note that all of our hybrid-DFT computed interlayer distances for all materials (Figure 1) Δd_{12} are negative. This means that, according to our hybrid-DFT computations, the contraction always happens between the first and second surface layer for all BO_2-terminated ABO_3 perovskite (001) surfaces (Table 5). Oppositely, according to our hybrid-DFT computations, there is always expansion between the second and third surface layer Δd_{23} (Figure 1) for all of our hybrid-DFT computed BO_2-terminated ABO_3 perovskite (001) surfaces (Table 5).

Table 4. Atomic relaxation magnitudes (in % of the a_0) for the AO-terminated $PbTiO_3$, $BaTiO_3$, $SrTiO_3$, $PbZrO_3$ and $SrZrO_3$ (001) surfaces.

Solid		**$PbTiO_3$**	**$BaTiO_3$**	**$SrTiO_3$**	**$PbZrO_3$**	**$SrZrO_3$**
Layer	Ion	PbO-t.	BaO-t.	SrO-t.	PbO-t.	SrO-t.
1	A	−3.82	−1.99	−4.84	−5.69	−7.63
	O	−0.31	−0.63	+0.84	−2.37	−0.86
2	B	+3.07	+1.74	+1.75	+0.57	+0.86
	O	+2.30	+1.40	+0.77	+0.09	−0.05
3	A	-	-	-	−0.47	−1.53
	O	-	-	-	−0.47	−0.45

Table 5. Our hybrid-DFT computed surface rumpling s as well as relative displacements Δd_{ij} for BO_2-terminated $PbTiO_3$, $BaTiO_3$, $SrTiO_3$, $PbZrO_3$ and $SrZrO_3$ (001) surfaces in (% of a_0). Relevant experimental data are listed in Table 5 for comparison purposes.

Solid	**Functional**	**Termination**	**s**	**Δd_{12}**	**Δd_{23}**
$PbZrO_3$	B3LYP	ZrO_2	+0.38	−6.73	+4.83
$SrZrO_3$	B3LYP	ZrO_2	−0.72	−4.19	+2.85
	LDA [131]	ZrO_2	−0.7	−6.1	+4.2
$PbTiO_3$	B3PW	TiO_2-term.	+3.12	−8.13	+5.32
$BaTiO_3$	B3PW	TiO_2-term.	+2.73	−5.59	+2.51
$SrTiO_3$	B3PW	TiO_2-term.	+2.12	−5.79	+3.55
	LEED [132]	TiO_2-term.	+2.1 ± 2	+1 ± 1	−1 ± 1
	RHEED [133]	TiO_2-term.	+2.6	+1.8	+1.3

As we can see from our hybrid-DFT computation results, collected in Table 6, the B-O atom chemical bond populations on the BO_2-terminated $PbZrO_3$, $SrZrO_3$, $PbTiO_3$, $BaTiO_3$ and $SrTiO_3$ perovskite (001) surfaces (+0.116*e*, +0.114*e*, +0.114*e*, +0.126*e*, +0.118*e*, respectively) are always larger than the B-O chemical bond population at the same perovskite bulk (+0.106*e*, +0.092*e*, +0.098*e*, +0.098*e*, +0.088*e*, respectively). As we can see from Table 6, the largest chemical bond population is between the Ti-O atoms (+0.126*e*) on the TiO_2-terminated $BaTiO_3$ (001) surface, whereas the smallest chemical bond population (+0.114*e*) is between the Zr-O and Ti-O atoms on the $SrZrO_3$, as well as the $BaTiO_3$, ZrO_2 and TiO_2-terminated (001), surfaces. It is worthwhile to note that the Ti atom's effective charges on the TiO_2-terminated $PbTiO_3$, $BaTiO_3$ and $SrTiO_3$ (001) surfaces (+2.279*e*, +2.307*e* and +2.291*e*, respectively) are reduced with regard to the Ti atom's effective charges in the $PbTiO_3$, $BaTiO_3$ and $SrTiO_3$ bulk (+2.341*e*, +2.367*e* and +2.351*e*, respectively). Just the opposite situation occurs for the $PbZrO_3$ and $SrZrO_3$ perovskites, wherein the Zr atom's effective charge on the ZrO_2-terminated $PbZrO_3$ and $SrZrO_3$ (001) surfaces (+2.165*e* and +2.196*e*, respectively) is larger than in the $PbZrO_3$ and $SrZrO_3$ bulk matrixes (+2.111*e* and +2.174*e*, respectively) (Table 6).

Table 6. Our hybrid-DFT computed atomic displacement absolute magnitudes D (in Å) and the effective charges Q (in e), as well as the chemical bond populations P (in e), for BO_2-terminated $PbZrO_3$, $SrZrO_3$, $PbTiO_3$, $BaTiO_3$ and $SrTiO_3$ (001) surfaces.

			$PbZrO_3$	$SrZrO_3$	$PbTiO_3$	$BaTiO_3$	$SrTiO_3$
Layer	**Prop.**	**Ion**	**ZrO_2-t.**	**ZrO_2-t.**	**TiO_2-t.**	**TiO_2-t.**	**TiO_2-t.**
1	D	B	−0.100	−0.058	−0.111	−0.123	−0.088
	Q		+2.165	+2.196	+2.279	+2.307	+2.291
	P		+0.116	+0.114	+0.114	+0.126	+0.118
	D	O	−0.084	−0.088	+0.012	−0.014	−0.005
	Q		−1.171	−1.277	−1.184	−1.280	−1.296
	P		+0.046	−0.002	+0.044	−0.038	−0.014
2	D	A	+0.184	+0.118	+0.209	+0.101	+0.139
	Q		+1.357	+1.869	+1.275	+1.767	+1.850
	P		+0.022	+0.002	+0.008	−0.030	−0.008
	D	O	+0.044	+0.038	+0.050	+0.015	+0.022
	Q		−1.103	−1.287	−1.167	−1.343	−1.365
	P		+0.098	+0.094	+0.080	+0.090	+0.080
3	D	B	−0.020	−0.001	-	-	-
	Q		+2.116	+2.172	+2.335	+2.365	+2.348
	P		+0.124	+0.102	+0.108	+0.104	+0.096
	D	O	−0.012	−0.002	-	-	-
	Q		−1.148	−1.331	−1.207	−1.371	−1.384
	P		+0.036	+0.002	+0.018	−0.034	−0.010

Our hybrid-DFT computed (001) surface cleavage and relaxation, as well as surface energies, for $PbTiO_3$, $BaTiO_3$, $SrTiO_3$, $PbZrO_3$ and $SrZrO_3$ perovskites are collected in Table 7. As we can see from Table 7, the largest cleavage energy is for the $SrZrO_3$ perovskite (001) surface (1.56 eV), whereas the smallest cleavage energy is for the $PbTiO_3$ perovskite (001) surface (1.02 eV) (Table 7). The largest surface relaxation energy is for the SrO-terminated $SrZrO_3$ perovskite (001) surface (−0.43), but the smallest surface relaxation energy is for the BaO-terminated $BaTiO_3$ (001) surface and is only (−0.11 eV) (Table 7). Finally, our hybrid-DTT computed surface energy is largest for the ZrO_2-terminated $SrZrO_3$ (001) surface (1.24 eV). Oppositely, our hybrid-DFT computed surface energy is the smallest for the TiO_2-terminated $PbTiO_3$ (001) surface and is only (0.74 eV). The largest energy difference (0.12 eV) for single perovskite (001) surfaces with different terminations is between the TiO_2-terminated $BaTiO_3$ (001) surface (1.07 eV) and the BaO-terminated $BaTiO_3$ (001) surface (1.19 eV). This means, that, for all of our hybrid-DFT computed $PbTiO_3$, $BaTiO_3$, $SrTiO_3$, $PbZrO_3$ and $SrZrO_3$ (001) surfaces, the surface energies for one perovskite's both surface terminations are rather close, and thereby both BO_2 and AO (001) surface terminations may exist simultaneously for all our hybrid-DFT computed ABO_3 perovskites (Table 7).

Our B3PW computed bulk band gaps (Figure 4) for $PbTiO_3$, $BaTiO_3$ and $SrTiO_3$ perovskite bulk (4.32 eV, 3.55 eV and 3.96 eV, respectively) are in fair agreement with the available experimental data [124,125,134] (Table 8). As we can see from Table 8 and Figures 5 and 6, our B3PW computed (001) surface band gaps for all three perovskites and both (001) surface terminations are always reduced with respect to the $PbTiO_3$, $BaTiO_3$ and $SrTiO_3$ bulk. Namely, our hybrid-DFT computed TiO_2-terminated $PbTiO_3$, $BaTiO_3$ and $SrTiO_3$ (001) surface band gaps are equal to 3.18 eV, 2.96 eV (Figure 5) and 3.95 eV, respectively. At the same time, our hybrid-DFT computed AO-terminated $PbTiO_3$, $BaTiO_3$ and $SrTiO_3$ (001) surface band gaps are equal to 3.58 eV, 3.49 eV (Figure 6) and 3.72 eV, respectively, and are also smaller than the respective bulk band gap values at Γ-point (Table 8).

Table 7. Our hybrid-DFT computed cleavage and relaxation, as well as surface energies, for $PbTiO_3$, $BaTiO_3$, $SrTiO_3$, $PbZrO_3$ and $SrTiO_3$ (001) surfaces (in eV per surface cell).

Surface	Termination	$E_{cleavage}$	$E_{relaxation}$	$E_{surface}$
$PbTiO_3$ (001)	TiO_2	1.02	−0.28	0.74
	PbO		−0.19	0.83
$BaTiO_3$ (001)	TiO_2	1.30	−0.23	1.07
	BaO		−0.11	1.19
$SrTiO_3$ (001)	TiO_2	1.39	−0.16	1.23
	SrO		−0.24	1.15
$PbZrO_3$ (001)	ZrO_2	1.20	−0.27	0.93
	PbO		−0.20	1.00
$SrZrO_3$ (001)	ZrO_2	1.56	−0.32	1.24
	SrO		−0.43	1.13

Table 8. Our hybrid-DFT computed direct Γ-Γ band gaps (in eV) for $PbTiO_3$, $BaTiO_3$ and $SrTiO_3$ perovskite bulk, as well as their BO_2 and AO-terminated (001) surfaces. The experimental $PbTiO_3$, $BaTiO_3$ and $SrTiO_3$ bulk Γ-Γ band gaps are listed for comparison purposes.

Termination	$PbTiO_3$ (Γ-Γ) Gap	$BaTiO_3$ (Γ-Γ) Gap	$SrTiO_3$ (Γ-Γ) Gap
Bulk	4.32 eV	3.55 eV	3.96 eV
TiO2-term. (001)	3.18 eV	2.96 eV	3.95 eV
AO-term. (001)	3.58 eV	3.49 eV	3.72 eV
Experiment	3.4 eV [134]	3.2 eV [125]	3.75 eV [124]

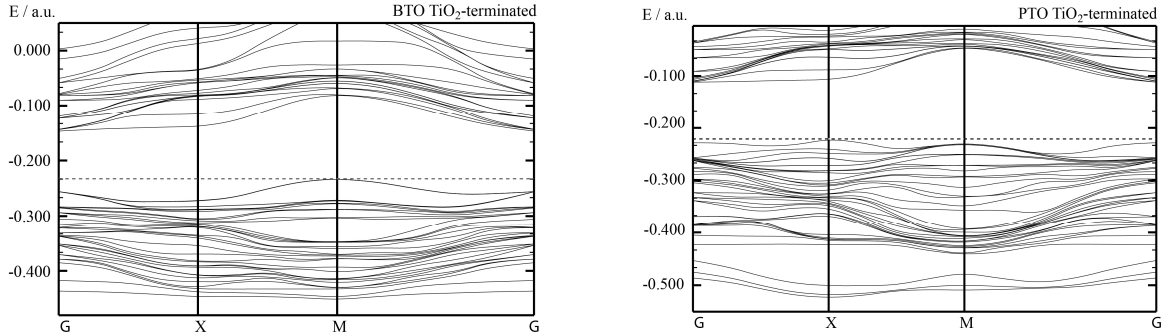

Figure 5. Our B3PW computed band gaps for TiO_2-terminated (001) surfaces for: (**a**) $BaTiO_3$ perovskite and (**b**) $PbTiO_3$ perovskite.

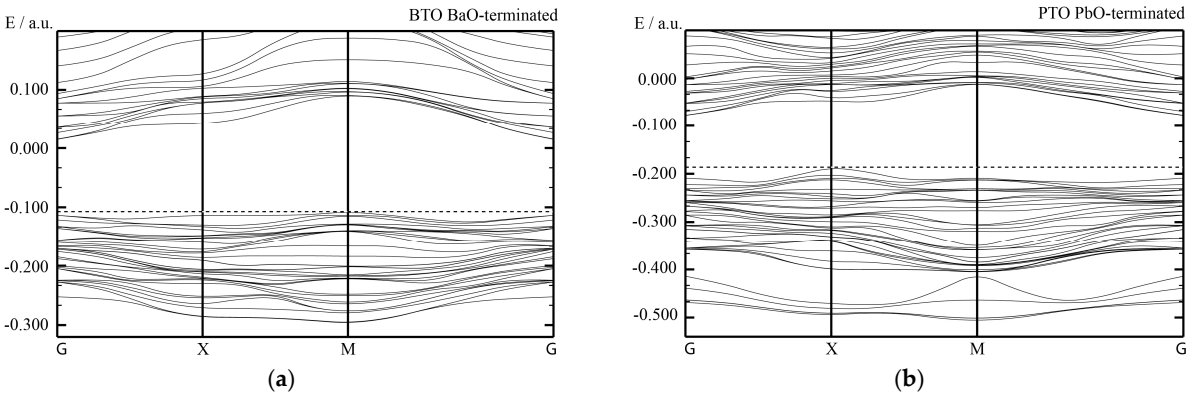

Figure 6. Our B3PW computed band gaps for AO-terminated (001) surfaces for: (**a**) $BaTiO_3$ perovskite and (**b**) $PbTiO_3$ perovskite.

3.2. $BaTiO_3/SrTiO_3$, $PbTiO_3/SrTiO_3$ and $SrZrO_3/PbZrO_3$ (001) Interfaces

In order to start our hybrid-DFT computations for BTO/STO, PTO/STO and SZO/PZO (001) heterostructures, we computed their joint lattice constants. Our hybrid-DFT computed joint lattice constant for BTO/STO (001) interface is equal to 3.958 Å. This joint BTO/STO (001) interface joint lattice constant was computed for the system containing an 11-layer thick STO substrate, as well as 10 BTO monolayers augmented on both sides of the STO substrate (Figure 3). Thereby, our B3PW computed thickest BTO/STO (001) interface contained 31 monolayers, as well as 78 atoms (Figure 3) [135]. Using a similar model for the PTO/STO (001) thickest interface, our B3PW computed joint lattice constant for this system is equal to 3.91 Å. Finally, our hybrid-DFT computed SZO/PZO (001) interface joint lattice constant for the system containing an 11-layer thick SZO substrate, as well as 10 PZO monolayers augmented symmetrically on both sides of the substrate, is equal to 4.167 Å.

In our hybrid-DFT (001) heterostructure computations, we relaxed all atomic positions only alongside the z-axis, due to the symmetry constraints for the cubic ABO_3 perovskite matrixes. We computed the atomic shifts Δz regarding the averaged coordinate z of the former atomic layer as described in Equation (4). As we can see from Figure 7, our B3PW computed upper $SrTiO_3$ substrate (001) layer, which contains Ti and O atoms (x = 0) in (Figure 7), relaxes very strongly inside (−5.95% of a_0). According to our B3PW computations, upper BTO (001) layer atoms, augmented on the STO 11-layer (001) substrate, always very strongly shifts (Δz) inwards (x = 1–10 in Figure 7). It is worthwhile to note that the BTO upper-layer atoms inwards-relaxation numerical value Δz considerably depends on the number of the STO (001) 11-layer substrate augmented BTO (001) layers.

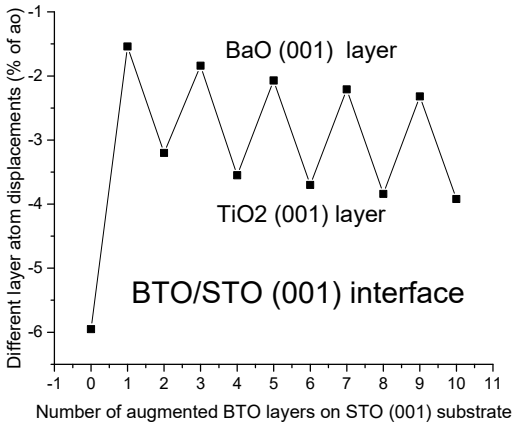

Figure 7. Our hybrid-DFT computed upper-layer atomic displacement magnitudes Δz (% of joint lattice constant a_0) for an 11-layer STO (001) substrate (x = 0) and for 10 augmented BTO layers (x = 1–10).

In the case of one augmented BTO (001) layer, consisting of the BaO atoms, the atom relaxation magnitude Δz is equal to −1.54% of the joint lattice constant a_0 (Figures 3 and 7). For two augmented BTO (001) layers, where the upper layer contains TiO_2 atoms, the upper-layer atom relaxation magnitude Δz is equal to (−3.20% of a_0) (Figure 7). For three augmented BTO (001) layers, the upper BaO layer atom relaxation magnitude Δz is equal to (−1.84% of a_0), for 4 layers (−3.55% of a_0), for five layers (−2.07% of a_0), for six layers (−3.70% of a_0), for seven layers (−2.21% of a_0), for eight layers (−3.84% of a_0), for nine layers (−2.32% of a_0) and finally, for ten augmented BTO (001) layers, the upper TiO_2 layer atom relaxation magnitude Δz is equal to (−3.92% of a_0) (Figure 7).

As we can see from Figure 8, for one augmented PTO (001) layer (x = 1), consisting of the PbO atoms, on the 11-layer STO (001) substrate (x = 0 for the substrate upper layer TiO_2 atoms relaxation magnitude Δz), the upper layer PbO atoms' relaxation magnitude Δz is equal to (−6.01% of a_0). For two augmented PTO (001) layers, the upper layer consists of TiO_2 atoms (x = 2), and their relaxation magnitude Δz is equal to (−7.76% of a_0). For three augmented PTO (001) layers (x = 3), the upper layer consists of PbO atoms, and their relaxation magnitude Δz is equal to (−6.97% of a_0). As we can see from Figure 8, for

four augmented PTO (001) layers (x = 4), the upper TiO_2 atoms containing layer atoms' relaxation magnitude Δz is equal to (−8.25% of a_0). For (x = 5), the upper augmented PTO (001) layer atom relaxation magnitude Δz is equal to (−7.26% of a_0), for (x = 6) (−8.38% of a_0), for (x = 7) (−7.34% of a_0), for (x = 8) (−8.54% of a_0), for (x = 9) (−7.42% of a_0) and for (x = 10) (−8.54% of a_0) (Figure 8).

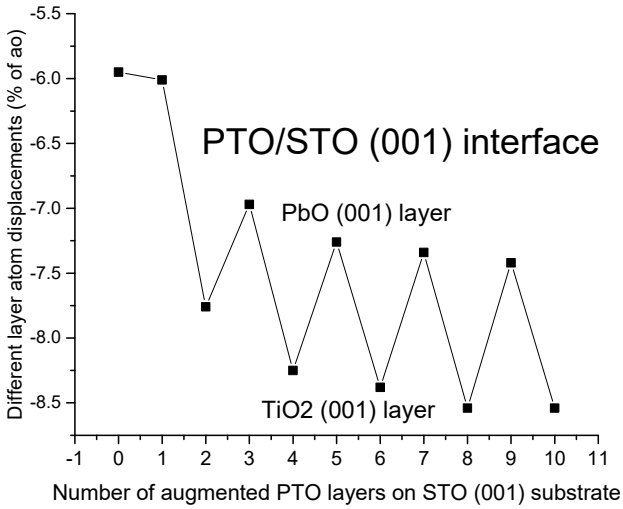

Figure 8. Our hybrid-DFT computed upper-layer atomic displacement magnitudes Δz (% of joint lattice constant a_0) for the 11-layer STO (001) substrate (x = 0) and for 10 augmented PTO layers (x= 1–10).

As we can see from Figure 9, our hybrid-DFT computed Γ-Γ band gap for the PTO/STO (001) interface, containing an 11-layer STO (001) substrate as well as a PbO (001) layer (x = 1), augmented on both sides of this substrate, is equivalent to 3.45 eV. For two PTO (001) layers, augmented from both sides on the 11-layer STO (001) substrate, the whole PTO/STO (001) interface system is terminated by the TiO_2 (001) layers from both sides and has a Γ-Γ band gap equal to 3.18 eV (Figure 9). For three PTO (001) layers, augmented on the STO (001) substrate, the whole PTO/STO (001) interface is terminated by the PbO-terminated (001) layer from both sides and has a Γ-Γ band gap equal to 3.25 eV. As we can see from Figure 9, for four augmented PTO (001) layers (x = 4), the Γ-Γ band gap of PTO/STO (001) interface is equal to 3.17 eV, for 5 augmented layers (3.08 eV), for 6 layers (3.05 eV), for 7 layers (2.99 eV), for 8 layers (2.99 eV), for 9 layers (2.94 eV) and, finally, for 10 augmented PTO (001) layers, the Γ-Γ band gap of PTO/STO (001) interface is equal to (2.93 eV).

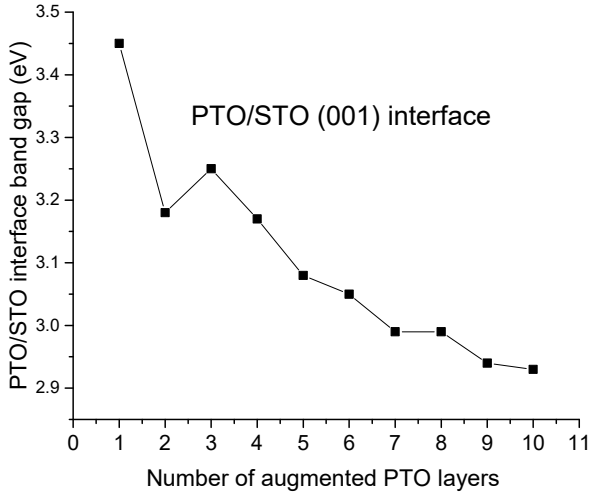

Figure 9. Our hybrid-DFT computed Γ-Γ band gap (in eV) for the PTO/STO (001) interface depending on the number of PTO (001) layers (x = 1–10) augmented on the 11-layer symmetrical TiO_2-terminated $SrTiO_3$ (001) substrate.

As we can see from Figure 10a,b, our hybrid-DFT computed Γ-Γ band gap for BTO/STO, as well as SZO/PZO (001) interface Γ-Γ band gap, very strongly depends on the upper augmented layer BO_2- or AO-termination but considerably less so on the number of augmented (001) layers.

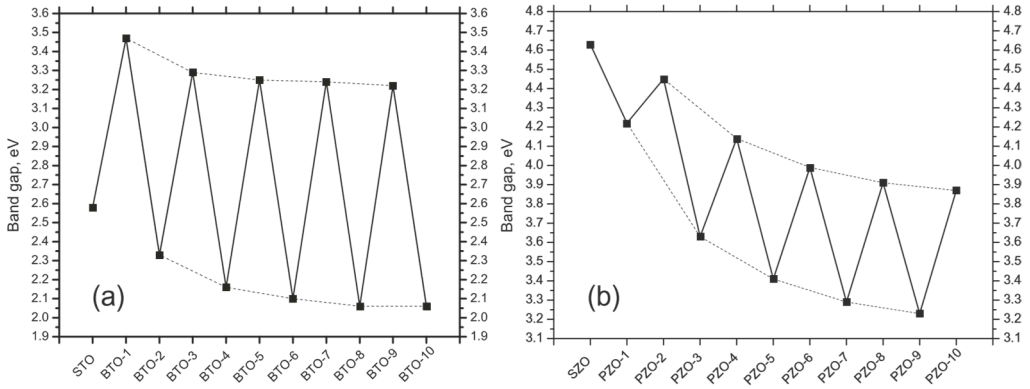

Figure 10. Our B3PW computed Γ-Γ band gap (in eV) for BTO/STO (**a**) and PZO/SZO (**b**) (001) interfaces, containing an 11-layer STO or SZO substrate as well as from 1 to 10 augmented BTO or PZO layers, respectively. Dashed lines serve as a guide for the eyes.

4. Conclusions

According to our hybrid-DFT computations for BO_2- and AO-terminated $PbTiO_3$, $BaTiO_3$, $SrTiO_3$, $PbZrO_3$ and $SrZrO_3$ (001) surfaces, in most cases, the upper-layer ions relax inwards, towards the bulk, whereas the second-layer ions shift upwards. It is worthwhile to also note that independent calculation results of other authors for ABO_3 perovskite material's neutral (001) surfaces confirm this systematic trend, that the upper layer ions, in most cases, relax inwards, whereas the second layer ions, again, in most cases, relax upwards [4,9,20,49,50,54,66,67,135–138].

Our hybrid-DFT computed surface rumpling *s* for the BO_2-terminated ABO_3 perovskite (001) surfaces (Table 5) is positive for most computed ABO_3 perovskites, such as $PbZrO_3$, $PbTiO_3$, $BaTiO_3$ and $SrTiO_3$ (+0.38, +3.12, +2.73 and +2.12, respectively). Furthermore, the experimentally detected surface rumpling *s* for the TiO_2-terminated $SrTiO_3$ (001) surface matrix by two different experimental methods (LEED [132] and RHEED [133]) is positive (Table 5). Moreover, the agreement between our B3PW computed surface rumpling *s* for the TiO_2-terminated $SrTiO_3$ (001) surface (+2.12) and LEED [131] experimentally detected respective $SrTiO_3$ (001) surface rumpling *s* (+2.1 ± 2) is almost perfect (Table 5). Nevertheless, there is a single exception to this systematic trend. Namely, our hybrid-DFT computed surface rumpling *s* for the ZrO_2-terminated $SrZrO_3$ (001) surface is negative (−0.72) and is in line with another ab initio calculation result performed by Wang et al. [131] (−0.70).

Our hybrid-DFT computed B-O atom chemical bond population values in the bulk of $PbTiO_3$ (+0.098*e*), $BaTiO_3$ (+0.098*e*), $SrTiO_3$ (+0.088*e*), $PbZrO_3$ (+0.106*e*) and $SrZrO_3$ (+0.092*e*) perovskites are considerably enhanced on their BO_2-terminated $PbTiO_3$ (+0.114*e*), $BaTiO_3$ (+0.126*e*), $SrTiO_3$ (+0.118*e*), $PbZrO_3$ (+0.116*e*) and $SrZrO_3$ (+0.114*e*) (001) surfaces (Table 6). Our hybrid-DFT computed BO_2- and AO-terminated (001) surface energies for $PbTiO_3$ (0.74 and 0.83 eV), $BaTiO_3$ (1.07 and 1.19 eV), $SrTiO_3$ (1.23 and 1.15 eV), $PbZrO_3$ (0.93 and 1.00 eV) and $SrZrO_3$ (1.24 and 1.13 eV) are comparable for both (001) surface terminations (Table 7). Thereby, both BO_2- and AO-terminated (001) surfaces may co-exist in ABO_3 perovskite matrices. It is worthwhile to note that our hybrid-DFT computed ABO_3 perovskite (001) surface energies are always smaller than the (011) [1,2] and especially the (111) [128] surface energies. This means, that, according to our hybrid-DFT computations, the ABO_3 perovskite (001) surfaces are always the most stable, whereas the (011) and especially the (111) ABO_3 perovskite surfaces are considerably less stable. Finally, our hybrid-DFT computed bulk Γ-Γ band gaps for $PbTiO_3$, $BaTiO_3$ and $SrTiO_3$ perovskites are

in fair agreement with the experimentally available data. For BO2- and AO-terminated $PbTiO_3$, $BaTiO_3$ and $SrTiO_3$ (001) surfaces (Table 8), the band gaps are always reduced with regard to the respective bulk Γ-Γ band gaps.

For our B3PW computed BTO/STO as well as PTO/STO (001) interfaces, the average augmented upper-layer atom relaxation magnitudes increased by the number of augmented BTO or PTO (001) layers but always independently from the number of augmented layers, which were stronger for TiO_2-terminated than BaO- or PbO-terminated upper augmented layers. All of our B3PW computed PTO/STO (001) interface upper augmented layer average atom displacement magnitudes Δz are between (-6.01% of a_0) for the first augmented layer and (-8.54% of a_0) for 10 augmented layers. In contrast to the PTO/STO (001) interfaces, for our hybrid-DFT computed BTO/STO (001) interfaces, the upper augmented layer average atom displacement magnitudes Δz are considerably smaller, and they are in the range between the (-1.54% of a_0 (1 layer) to -3.92% of a_0 (10 layers), respectively). Our B3PW computed BTO/STO, as well as SZO/PZO (001) interface Γ-Γ band gaps, very strongly depends on the upper augmented layer BO_2- or AO-termination but considerably less so on the number of augmented (001) layers [135,139].

Summing up, all of our hybrid-DFT computed BTO/STO and PTO/STO, as well as PZO/SZO (001) heterostructures, are semiconducting. In general agreement with available experimental data [84], according to our hybrid-DFT computations, the (001) interface layer does not considerably influence the electronic structure of our studied heterostructures. At the same time, the termination of the deposited BTO and PTO, as well as PZO (001), thin films atop STO or SZO (001) substrates, respectively, may shift the band edges regarding the vacuum level and thereby reduce the (001) heterostructure band gap [84].

Author Contributions: Conceptualization, R.J. and A.I.P.; methodology, R.I.E.; software, S.P.; validation, R.I.E., R.J. and D.B.; formal analysis, A.I.P.; investigation, J.P.; resources, D.B.; data curation, S.P.; writing—original draft preparation, R.I.E., J.P., D.B., S.P., R.J. and A.I.P.; writing—review and editing, R.I.E., J.P., A.I.P., R.J., S.P. and D.B; visualization, S.P.; funding acquisition, J.P. All authors have read and agreed to the published version of the manuscript.

Funding: We acknowledge the financial support from the funder—Latvian Council of Science. The funding number is: Grant No. LZP-2020/1-0345. The Institute of Solid State Physics, University of Latvia (Latvia), as the Centre of Excellence, has received funding from the European Unions Horizon 2020 Framework Programme H2020-WIDESPREAD01-2016-2017-Teaming Phase2 under Grant Agreement No. 739508, project CAMART-2.

Data Availability Statement: Not applicable.

Conflicts of Interest: The authors declare no conflict of interest.

References

1. Eglitis, R.I.; Vanderbilt, D. *Ab initio* calculations of the atomic and electronic structure of $CaTiO_3$ (001) and (011) surfaces. *Phys. Rev. B* **2008**, *78*, 155420. [CrossRef]
2. Eglitis, R.I.; Vanderbilt, D. *Ab initio* calculations of $BaTiO_3$ and $PbTiO_3$ (001) and (011) surface structures. *Phys. Rev. B* **2007**, *76*, 155439. [CrossRef]
3. Erdman, N.; Poeppelmeier, K.R.; Asta, M.; Warschkov, O.; Ellis, D.E.; Marks, L.D. The structure and chemistry of the TiO_2-rich surface of $SrTiO_3$ (001). *Nature* **2002**, *419*, 55–58. [CrossRef]
4. Dawber, M.; Rabe, K.M.; Scott, J.F. Physics of thin-film ferroelectric oxides. *Rev. Mod. Phys.* **2005**, *77*, 1083–1130. [CrossRef]
5. Piyanzina, I.I.; Pavlov, D.P.; Jagličić, Z.; Shulyaev, D.A.; Tayurskii, D.A.; Kabanov, V.V.; Mamin, R.F. Structural and magnetic properties of ferroelectric/dielectric $BaTiO_3/LaMnO_3$ and $BaTiO_3/SrTiO_3$ heterostructures. *Ferroelectrics* **2021**, *575*, 144–150. [CrossRef]
6. Eglitis, R.I.; Kleperis, J.; Purans, J.; Popov, A.I.; Jia, R. *Ab initio* calculations of $CaZrO_3$ (011) surfaces: Systematic trends in polar (011) surface calculations of ABO_3 perovskites. *J. Mater. Sci.* **2020**, *55*, 203–217. [CrossRef]
7. Danyushkina, L.A.; Khaliullina, A.S.; Kuimov, V.M.; Osinkin, D.A.; Antonov, B.D.; Pankratov, A.A. Influence of modification of chemical solution deposition on morphology and conductivity of $CaZr_{0.9}Y_{0.1}O_{3-\delta}$ films. *Solid State Ion.* **2019**, *329*, 1–7. [CrossRef]
8. Eglitis, R.I.; Popov, A.I. *Ab initio* calculations for the polar (001) surfaces of $YAlO_3$. *Nucl. Instr. Meth. B* **2018**, *434*, 1–5. [CrossRef]
9. Brik, M.G.; Ma, C.G.; Krasnenko, V. First-principles calculations of the structural and electronic properties of the cubic $CaZrO_3$ (001) surfaces. *Surf. Sci.* **2013**, *608*, 146–153. [CrossRef]

10. Eglitis, R.I. Comparative *ab initio* calculations of $SrTiO_3$ and $CaTiO_3$ polar (111) surfaces. *Phys. Stat. Sol. B* **2015**, *252*, 635–642. [CrossRef]
11. Ahmadi, F.; Aragi, H. Coexistence of magnetism and ferroelectricity in $(PbTiO_3)_m/(BaTiO_3)_n$ superlattices. *Superlattices Microstruct.* **2020**, *140*, 106427. [CrossRef]
12. Jia, W.; Vikhnin, V.S.; Liu, H.; Kapphan, S.; Eglitis, R.; Usvyat, D. Critical effects in optical response due to charge transfer vibronic excitions and their structure in perovskite-like systems. *J. Lumin.* **1999**, *83*, 109–113. [CrossRef]
13. Zhang, X.; Demkov, A.A.; Li, H.; Hu, X.; Wei, Y.; Kulik, J. Atomic and electronic structure of the $Si/SrTiO_3$ interface. *Phys. Rev. B* **2003**, *68*, 125323. [CrossRef]
14. Eglitis, R.I.; Purans, J.; Popov, A.I.; Bocharov, D.; Chekhovska, A.; Jia, R. *Ab initio* computations of O and AO as well as ReO_2, WO_2 and BO_2-terminated ReO_3, WO_3, $BaTiO_3$, $SrTiO_3$ and $BaZrO_3$ (001) surfaces. *Symmetry* **2022**, *14*, 1050. [CrossRef]
15. Raza, S.; Zhang, R.; Zhang, N.; Li, Z.; Liu, L.; Zhang, F.; Wang, D.; Jia, C.L. $ATiO_3/TiO$ (A=Pb, Sn) superlattice: Bridging ferroelectricity and conductivity. *Comput. Condens. Matter* **2020**, *25*, e00491. [CrossRef]
16. Borstel, G.; Eglitis, R.I.; Kotomin, E.A.; Heifets, E. Modelling of defects and surfaces in perovskite ferroelectrics. *Phys. Stat. Sol. B* **2003**, *236*, 253–264. [CrossRef]
17. Cohen, R.E. Origin of ferroelectricity in perovskite oxides. *Nature* **1992**, *358*, 136–138. [CrossRef]
18. Zhong, W.; Vanderbilt, D.; Rabe, K.M. Phase transitions in $BaTiO_3$ from first principles. *Phys. Rev. Lett.* **1994**, *73*, 1861–1864. [CrossRef]
19. Eglitis, R.I.; Kotomin, E.A.; Borstel, G. Quantum chemical modelling of perovskite solid solutions. *J. Phys. Condens. Matter* **2000**, *12*, L431–L434. [CrossRef]
20. Sambrano, J.R.; Longo, V.M.; Longo, E.; Taft, C.A. Electronic and structural properties of the (001) $SrZrO_3$ surface. *J. Mol. Struct. THEOCHEM* **2007**, *813*, 49–56. [CrossRef]
21. Kennedy, B.J.; Howard, C.J. High-temperature phase transition in $SrZrO_3$. *Phys. Rev. B* **1999**, *59*, 4023–4027. [CrossRef]
22. Maniwa, H.; Sawaguchi, E.; Hoshino, S. Antiferroelectric structure of lead zirconate. *Phys. Rev.* **1951**, *83*, 1078.
23. Shirane, G.; Sawaguchi, E.; Takagi, Y. Dielectric properties of lead zirconate. *Phys. Rev.* **1951**, *84*, 476–481. [CrossRef]
24. Wang, H.; Liu, Y.; Yang, T.; Zhang, S. Ultra high energy-storage density in antiferroelectric ceramics with field-induced multiphase transitions. *Adv. Funct. Mater.* **2019**, *29*, 1807321. [CrossRef]
25. Chen, M.J.; Ning, X.K.; Wang, S.F.; Fu, G.S. Significant enhancement of energy storage density and polarization in self-assembled $PbZrO_3$: NiO nano-columnar composite films. *Nanoscale* **2019**, *11*, 1914–1920. [CrossRef]
26. Zhang, S.; Li, F. High performance ferroelectric relaxor-$PbTiO_3$ single crystals: Status and perspective. *Appl. Phys. Rev.* **2012**, *111*, 031301. [CrossRef]
27. Sebastian, M.T. Polymer-Ceramic Composites of O-3 Connectivity for Circuits in Electronics: A Review. *Int. J. Appl. Ceram. Technol.* **2010**, *7*, 415–434. [CrossRef]
28. Tan, G.; Wang, S.; Zhu, Y.; Zhou, L.; Yu, P.; Wang, X.; He, T.; Chen, J.; Mao, C.; Ning, C. Surface-selective preferential production of reactive oxygen species on piezoelectric ceramics for bacterial killing. *ACS Appl. Mater. Interfaces* **2016**, *8*, 24306–24309. [CrossRef]
29. Kumar, S.; Vaish, R.; Powar, S. Surface-selective bactericidal effect on poled ferroelectric materials. *J. Appl. Phys.* **2018**, *124*, 014901. [CrossRef]
30. Acosta, M.; Novak, N.; Rojas, V.; Patel, S.; Vaish, R.; Koruza, J.; Rossetti, G.A.; Rödel, J. $BaTiO_3$-based piezoelectrics: Fundamentals, current status, and perspectives. *Appl. Phys. Rev.* **2017**, *4*, 041305. [CrossRef]
31. Domen, K.; Kudo, A.; Onishi, T.; Kosugi, N.; Kuroda, H. Photocatalytic decomposition of water into hydrogen and oxygen over nickel (II) oxide-strontium titanate ($SrTiO_3$) powder. 1. Structure of the catalysts. *J. Phys. Chem.* **1986**, *90*, 292–295. [CrossRef]
32. Ahuja, S.; Kutty, T.R.N. Nanoparticles of $SrTiO_3$ prepared by gel to crystallite conversion and their photocatalytic activity in the mineralization of phenol. *J. Photochem. Photobiol. A Chem.* **1996**, *97*, 99–107. [CrossRef]
33. Samsonidze, G.; Kozinsky, B. Accelerated Screening of Thermoelectric Materials by First-Principles Computations of Electron-Phonon Scattering. *Adv. Energy Mater.* **2018**, *8*, 1800246. [CrossRef]
34. Guo, R.; Wang, X.; Kuang, Y.; Huang, B. First-principles study of anisotropic thermoelectric transport properties of IV-VI semiconductor compounds SnSe and SnS. *Phys. Rev. B* **2015**, *92*, 115202. [CrossRef]
35. Xi, L.; Zhang, Y.B.; Shi, Z.Y.; Yang, J.; Shi, X.; Chen, L.D.; Zhang, W.; Yang, J.; Sing, D.J. Chemical bonding, conductive network, and thermoelectric performance of the ternary semi conductors Cu_2SnX_3 (X = Se, S) from first principles. *Phys. Rev. B* **2012**, *86*, 155201. [CrossRef]
36. Tian, Z.; Garg, J.; Esfarjani, K.; Shiga, T.; Shiomi, J.; Chen, G. Phonon conduction in PbSe, PbTe, and $PbTe_{1-x}Se_x$ from first principles calculations. *Phys. Rev. B* **2012**, *85*, 184303. [CrossRef]
37. Orhan, E.; Pontes, F.M.; Pinteiro, C.D.; Boschi, T.M.; Leite, E.R.; Pizani, P.S.; Beltrán, A.; Andrés, J.; Varela, J.A.; Longo, E. Origin of photoluminescence in SrTiO3: A combined experimental and theoretical study. *J. Solid State Chem.* **2004**, *177*, 3879–3885. [CrossRef]
38. Grigorjeva, L.; Millers, D.K.; Pankratov, V.; Williams, R.T.; Eglitis, R.I.; Kotomin, E.A.; Borstel, G. Experimental and theoretical studies of polaron optical properties in $KNbO_3$ perovskite. *Solid State Commun.* **2004**, *129*, 691–696. [CrossRef]
39. Devreese, J.T.; Fomin, V.M.; Pokatilov, E.P.; Kotomin, E.A.; Eglitis, R.; Zhukovskii, Y.F. Theory of bound polarons in oxide compounds. *Phys. Rev. B* **2001**, *63*, 184304. [CrossRef]

40. Leonelli, R.; Brebner, J.L. Evidence for bimolecular recombination in the luminescence spectra of $SrTiO_3$. *Solid State Commun.* **1985**, *54*, 505–507. [CrossRef]
41. Makarova, M.V.; Prokhorov, A.; Stupak, A.; Kopeček, J.; Drahokoupil, J.; Trepakov, V.; Dejneka, A. Synthesis and Magnetic Properties of Carbon Doped and Reduced $SrTiO_3$ Nanoparticles. *Crystals* **2022**, *12*, 1275. [CrossRef]
42. Meng, J.; Huang, Y.; Zhang, W.; Du, Z.; Zhu, Z.; Zou, G. Photoluminescence in nanocrystalline $BaTiO_3$ and $SrTiO_3$. *Phys. Lett. A* **1995**, *205*, 72–76. [CrossRef]
43. Rinnert, H.; Vergat, M.; Marchal, G.; Burneau, A. Intense visible photoluminescence in amorphous SiO_x and SiO_x:H films prepared by evaporation. *Appl. Phys. Lett.* **1998**, *72*, 3157. [CrossRef]
44. Scott, J.F. Status report on ferroelectric memory materials. *Integr. Ferroelectr.* **1998**, *20*, 15–23. [CrossRef]
45. Millis, A.J. Lattice effects in magnetoresistive manganese perovskites. *Nature* **1998**, *392*, 147–150. [CrossRef]
46. Wessels, B.W. Metal-organic chemical vapor deposition of ferroelectric oxide thin films for electronic and optical applications. *Annu. Rev. Mater. Sci.* **1995**, *25*, 525–546. [CrossRef]
47. Farlenkov, A.S.; Ananyev, M.V.; Eremin, V.A.; Porotnikova, N.M.; Kurumchin, E.K.; Melekh, B.T. Oxygen isotope exchange in doped calcium and barium zirconates. *Solid State Ion.* **2016**, *290*, 108–115. [CrossRef]
48. Ananyev, M.V.; Bershitskaya, N.M.; Plaksin, S.V.; Kurumchin, E.K. Phase equilibriums, oxygen exchange kinetics and diffusion in oxides $CaZr_{1-x}Sc_xO_{3-x/2-\delta}$. *Russ. J. Electrochem.* **2012**, *48*, 879–886. [CrossRef]
49. Celik, F.A. Electronic structure of two-dimensional-layered $PbTiO_3$ perovskite crystal: An extended tight-binding study based on DFT. *Bull. Mater. Sci.* **2022**, *45*, 108. [CrossRef]
50. Eglitis, R.I. *Ab initio* calculations of $SrTiO_3$, $BaTiO_3$, $PbTiO_3$, $CaTiO_3$, $SrZrO_3$, $PbZrO_3$ and $BaZrO_3$ (001), (011) and (111) surfaces as well as *F* centers, polarons, KTN solid solutions and Nb impurities therein. *Int. J. Mod. Phys. B* **2014**, *28*, 1430009. [CrossRef]
51. Noor, N.A.; Mahmood, Q.; Rashid, M.; Haq, B.V.; Laref, A.; Ahmad, S.A. *Ab-initio* study of thermodynamic stability, thermoelectric and optical properties of perovskites $ATiO_3$ (A = Pb, Sn). *J. Solid State Chem.* **2018**, *263*, 115–122. [CrossRef]
52. Shimada, T.; Tomoda, S.; Kitamura, T. *Ab initio* study of ferroelectricity in edged $PbTiO_3$ nanowires under axial tension. *Phys. Rev. B* **2009**, *79*, 024102. [CrossRef]
53. Zhang, J.M.; Pang, Q.; Xu, K.W.; Ji, V. First-principles study of the (110) polar surface of cubic $PbTiO_3$. *Comput. Mater. Sci.* **2009**, *44*, 1360–1365. [CrossRef]
54. Lazaro, S.D.; Longo, E.; Sambrano, J.R.; Beltrán, A. Structural and electronic properties of $PbTiO_3$ slabs: A DFT periodic study. *Surf. Sci.* **2004**, *552*, 149–159. [CrossRef]
55. Eglitis, R.I.; Purans, J.; Popov, A.I.; Jia, R. Tendencies in ABO_3 perovskite and SrF_2, BaF_2 and CaF_2 bulk and surface *F*-center *ab initio* computations at high symmetry cubic structure. *Symmetry* **2021**, *13*, 1920. [CrossRef]
56. Gao, H.; Yue, Z.; Liu, Y.; Hu, J.; Li, X. A first-principles study on the multiferroic property of two-dimensional $BaTiO_3$ (001) ultrathin film with surface Ba vacancy. *Nanomaterials* **2019**, *9*, 269. [CrossRef]
57. Eglitis, R.I.; Purans, J.; Gabrusenoks, J.; Popov, A.I.; Jia, R. Comparative *ab initio* calculation of ReO_3, $SrZrO_3$, $BaZrO_3$, $PbZrO_3$ and $CaZrO_3$ (001) surfaces. *Crystals* **2020**, *10*, 745. [CrossRef]
58. Zhong, M.; Zeng, W.; Liu, F.S.; Tang, B.; Liu, Q.J. First-principles study of the atomic structures, electronic properties, and surface stability of $BaTiO_3$ (001) and (011) surfaces. *Surf. Interface Anal.* **2019**, *51*, 1021–1032. [CrossRef]
59. Eglitis, R.I.; Purans, J.; Jia, R. Comparative Hybrid Hartree-Fock-DFT Calculations of WO_2-Terminated Cubic WO_3 as well as $SrTiO_3$, $BaTiO_3$, $PbTiO_3$ and $CaTiO_3$ (001) surfaces. *Crystals* **2021**, *11*, 455. [CrossRef]
60. Costa-Amaral, R.; Gohda, Y. First-principles study of the adsorption of 3d transition metals on BaO- and TiO_2-terminated cubic-phase $BaTiO_3$ (001) surfaces. *J. Chem. Phys.* **2020**, *152*, 204701. [CrossRef]
61. Sokolov, M.; Eglitis, R.I.; Piskunov, S.; Zhukovskii, Y.F. *Ab initio* hybrid DFT calculations of $BaTiO_3$ bulk and BaO-terminated (001) surface *F*-centers. *Int. J. Mod. Phys. B* **2017**, *31*, 1750251. [CrossRef]
62. Eglitis, R.I.; Piskunov, S. First principles calculations of $SrZrO_3$ bulk and ZrO_2-terminated (001) surface *F* centers. *Comput. Condens. Matter* **2016**, *7*, 1–6. [CrossRef]
63. Charlton, G.; Brennan, S.; Muryn, C.A.; McGrath, R.; Norman, D.; Turner, T.S.; Thorton, G. Surface relaxation of $SrTiO_3$ (001). *Surf. Sci.* **2000**, *457*, L376–L380. [CrossRef]
64. Liang, Y.; Bonnell, D.A. Atomic structures of reduced $SrTiO_3$ (001) surfaces. *Surf. Sci. Lett.* **1993**, *285*, L510–L516.
65. Castell, M.R. Scanning tunneling microscopy of reconstructions on the $SrTiO_3$ (001) surface. *Surf. Sci.* **2002**, *505*, 1–13. [CrossRef]
66. Evarestov, R.A.; Bandura, A.V.; Alexandrov, V.E. Hybrid HF-DFT comparative study of $SrZrO_3$ and $SrTiO_3$ (001) surface properties. *Phys. Stat. Sol. B* **2006**, *243*, 2756–2763. [CrossRef]
67. Iles, N.; Finocchi, F.; Khodja, K.D. A systematic study of ideal and double layered reconstructions of ABO_3 (001) surfaces (A = Sr, Ba; B = Ti, Zr) from first principles. *J. Phys. Condens. Matter* **2010**, *22*, 305001. [CrossRef]
68. Sopiha, K.V.; Malyi, O.I.; Persson, C.; Wu, P. Suppression of surface states at cubic perovskite (001) surfaces by CO_2 adsorption. *Phys. Chem. Chem. Phys.* **2018**, *20*, 18828–18836. [CrossRef]
69. Pilania, G.; Tan, D.Q.; Cao, Y.; Venkataramani, V.S.; Chen, Q.; Ramprasad, R. Ab initio study of antiferroelectric $PbZrO_3$ (001) surfaces. *J. Mater. Sci.* **2009**, *44*, 5249–5255. [CrossRef]
70. Ko, D.L.; Hsin, T.; Lai, Y.H.; Ho, S.Z.; Zheng, Y.; Huang, R.; Pan, H.; Chen, Y.C.; Chu, Y.H. High-stability transparent flexible energy storage based on $PbZrO_3$ muscovite heterostructure. *Nano Energy* **2021**, *87*, 106149. [CrossRef]

71. Guo, X.; Ge, J.; Ponchel, F.; Remiens, D.; Chen, Y.; Dong, X.; Wang, G. Effect of Sn substitution on the energy storage properties of high (001)-oriented $PbZrO_3$ thin films. *Thin Solid Film.* **2017**, *632*, 93–96. [CrossRef]
72. Qiao, L.; Song, C.; Sua, Y.; Fayaz, M.U.; Lu, T.; Yin, S.; Chen, C.; Xu, H.; Ren, T.L.; Pan, F. Observation of negative capacitance in antiferroelectric $PbZrO_3$ Films. *Nat. Commun.* **2021**, *12*, 4215. [CrossRef] [PubMed]
73. Delugas, P.; Filipetti, A.; Gadaleta, A.; Pallecchi, I.; Marre, D.; Fiorentini, V. Large band offset as a driving force of two-dimensional electron confinement: The case of $SrTiO_3/SrZrO_3$ interface. *Phys. Rev. B* **2013**, *88*, 115304. [CrossRef]
74. Piskunov, S.; Eglitis, R.I. First principles hybrid DFT calculations of $BaTiO_3/SrTiO_3$ (001) interface. *Solid State Ion.* **2015**, *274*, 29–33. [CrossRef]
75. Al-Aqtash, N.; Alsaad, A.; Sabirianov, R. Ferroelectric properties of $BaZrO_3/PbZrO_3$ and $SrZrO_3/PbZrO_3$ superlattices: An *ab-initio* study. *J. Appl. Phys.* **2014**, *116*, 074112. [CrossRef]
76. Eglitis, R.; Kruchinin, S.P. Ab initio calculations of ABO_3 perovskite (001), (011) and (111) nano-surfaces, interfaces and defects. *Mod. Phys. Lett. B* **2020**, *34*, 2040057. [CrossRef]
77. Qi, H.; Chen, X.; Benckiser, E.; Wu, M.; Cristiani, G.; Logvenov, G.; Keimer, B.; Kaiser, V. Formation mechanism of Ruddlesden-Popper faults in compressive-strained ABO_3 perovskite superlattices. *Nanoscale* **2021**, *13*, 20663–20669. [CrossRef] [PubMed]
78. Aso, R.; Kan, D.; Shimakawa, Y.; Kurata, H. Atomic level observation of octahedral distortions at the perovskite oxide heterointerface. *Sci. Rep.* **2013**, *3*, 2214. [CrossRef] [PubMed]
79. Piskunov, S.; Eglitis, R.I. Comparative ab initio calculations of $SrTiO_3/BaTiO_3$ and $SrZrO_3/PbZrO_3$ (001) heterostructures. *Nucl. Instr. Methods B* **2016**, *374*, 20–23. [CrossRef]
80. Fredrickson, K.D.; Demkov, A.A. Switchable conductivity at the ferroelectric interface: Nonpolar oxides. *Phys. Rev. B* **2015**, *91*, 115126. [CrossRef]
81. Eglitis, R.I.; Piskunov, S.; Zhukovskii, Y.F. *Ab initio* calculations of $PbTiO_3/SrTiO_3$ (001) heterostructures. *Phys. Stat. Sol. C* **2016**, *13*, 913–920.
82. Lebedev, A.I. Ground state and properties of ferroelectric superlattices based on crystals of the perovskite family. *Phys. Solid State* **2010**, *52*, 1448–1462. [CrossRef]
83. Lebedev, A.I. Band offsets in heterojunctions formed by oxides with cubic perovskite structure. *Phys. Solid State* **2014**, *56*, 1039–1047. [CrossRef]
84. Bi, Z.; Uberuaga, B.P.; Vernon, L.J.; Fu, E.; Wang, Y.; Li, N.; Wang, H.; Misra, A.; Jia, Q.X. Radiation damage in heteroepitaxial $BaTiO_3$ thin films on $SrTiO_3$ under Ne ion irradiation. *J. Appl. Phys.* **2013**, *113*, 023513. [CrossRef]
85. Stepkova, V.; Marton, P.; Setter, N.; Hlinka, J. Closed-circuit domain quadruplets in $BaTiO_3$ nanorods embedded in a $SrTiO_3$ film. *Phys. Rev. B* **2014**, *89*, 060101. [CrossRef]
86. Piyanzina, I.I.; Eyert, V.; Lysogorskiy, Y.V.; Tayurskii, D.A.; Kopp, T. Oxygen vacancies and hydrogen doping in $LaAlO_3/SrTiO_3$ heterostructures: Electronic properties and impact on surface and interface reconstruction. *J. Phys. Condens. Matter* **2019**, *31*, 295601. [CrossRef] [PubMed]
87. Piyanzina, I.I.; Pavlov, D.P.; Zagidullin, R.R.; Tayurskii, D.A.; Mamin, R.F. Structural and electronic properties of heterointerface composed of non-polar oxides: $SrTiO_3$ and ferroelectric $BaTiO_3$. *Ferroelectrics* **2019**, *542*, 7–12. [CrossRef]
88. Piyanzina, I.I.; Lysogorskiy, Y.V.; Tayurskii, D.A.; Mamin, R.F. Electronic Properties of a Two-Dimensional Electron Gas at the Interface between Transition Metal Complex Oxides. *Bull. Russ. Acad. Sci. Phys.* **2018**, *82*, 234–237. [CrossRef]
89. Nova, T.F.; Disa, A.S.; Fechner, M.; Cavalleri, A. Metastable ferroelectricity in optically strained $SrTiO_3$. *Science* **2019**, *364*, 1075–1079. [CrossRef] [PubMed]
90. Oliveira, M.C.; Ribeiro, R.A.P.; Longo, E.; Bomio, M.R.D.; Motta, F.V.; Lazaro, S.R.D. Temperature dependence on phase evolution in BaTiO3 polytypes studied using *ab initio* calculations. *Int. J. Quantum Chem.* **2020**, *120*, e26054. [CrossRef]
91. Zelezny, V.; Chvostova, D.; Simek, D.; Maca, F.; Masek, J.; Setter, N.; Huang, Y.H. The variation of $PbTiO_3$ bandgap at ferroelectric phase transition. *J. Phys. Condens. Matter* **2016**, *28*, 025501. [CrossRef] [PubMed]
92. Ligny, D.D.; Richet, P. High-temperature heat capacity and thermal expansion of perovskites. *Phys. Rev. B* **1996**, *53*, 3013–3022. [CrossRef]
93. Bungaro, C.; Rabe, K.M. Coexistence of antiferrodistortive and ferroelectric distortions at the $BaTiO_3$ (001) surface. *Phys. Rev. B* **2005**, *71*, 035420. [CrossRef]
94. Ghorbani, E.; Villa, L.; Erhart, P.; Klein, A.; Albe, K. Self-consistent calculations of charge self-trapping energies: A comparative study of polaron formation and migration in $PbTiO_3$. *Phys. Rev. Mater.* **2022**, *6*, 074410. [CrossRef]
95. Varley, J.B.; Janotti, A.; Franchini, C.; Walle, C.G.V. Role of self-trapping in luminescence and *p*-type conductivity of wide-band-gap oxides. *Phys. Rev. B* **2012**, *85*, 081109. [CrossRef]
96. Eglitis, R.I.; Kotomin, E.A.; Trepakov, V.A.; Kapphan, S.E.; Borstel, G. Quantum chemical modelling of electron polarons and 'green' luminescence in $PbTiO_3$ perovskite crystals. *J. Phys. Condens. Matter* **2002**, *14*, L647. [CrossRef]
97. Dovesi, R.; Saunders, V.R.; Roetti, C.; Orlando, R.; Zicovich-Wilson, C.M.; Pascale, F.; Civalleri, B.; Doll, K.; Harrison, N.M.; Bush, I.J.; et al. *CRYSTAL-2017 User Manual*; University of Torino: Torino, Italy, 2017.
98. Lee, C.; Yang, W.; Parr, R.G. Development of the Colle-Salvetti correlation-energy formula into a functional of the electron density. *Phys. Rev. B* **1988**, *37*, 785–789. [CrossRef] [PubMed]
99. Perdew, J.P.; Wang, Y. Accurate and simple density functional for the electronic exchange energy: Generalized gradient approximation. *Phys. Rev. B* **1986**, *33*, 8800–8802; Erratum in *Phys. Rev. B* **1989**, *40*, 3399. [CrossRef] [PubMed]

100. Perdew, J.P.; Wang, Y. Accurate and simple analytic representation of the electron-gas correlation energy. *Phys. Rev. B* **1992**, *45*, 13244–13249. [CrossRef]
101. Shi, H.; Eglitis, R.I.; Borstel, G. *Ab initio* calculations of the CaF_2 electronic structure and *F* centers. *Phys. Rev. B* **2005**, *72*, 045109. [CrossRef]
102. Vassilyeva, A.F.; Eglitis, R.I.; Kotomin, E.A.; Dauletbekova, A.K. *Ab initio* calculations of MgF_2 (001) and (011) surface structure. *Phys. B Condens. Matter* **2010**, *405*, 2125–2127. [CrossRef]
103. Rubloff, G.W. Far-Ultraviolet Reflectence Spectra and the Electronic Structure of Ionic Crystals. *Phys. Rev. B* **1972**, *5*, 662–684. [CrossRef]
104. Perdew, J.; Ernzerhof, M.; Burke, K. Rationale for mixing exact exchange with density functional approximations. *J. Chem. Phys.* **1996**, *105*, 9982. [CrossRef]
105. Perdew, J.P. Orbital functional for exchange and correlation: Self-interaction correction to the local density approximation. *Chem. Phys. Lett.* **1979**, *64*, 127–130. [CrossRef]
106. Dovesi, R.; Orlando, R.; Roetti, C.; Pisani, C.; Saunders, V.R. The Periodic Hartree-Fock Method and Its Implementation in the Crystal Code. *Phys. Stat. Sol. B* **2000**, *217*, 63–88. [CrossRef]
107. Lisitsyn, V.M.; Lisitsyna, L.A.; Popov, A.I.; Kotomin, E.A.; Abuova, F.U.; Akilbekov, A.; Maier, J. Stabilization of primary mobile radiation defects in MgF_2 crystals. *Nucl. Instr. Methods B* **2016**, *374*, 24–28. [CrossRef]
108. Heifets, E.; Kotomin, E.A.; Maier, J. Semi-empirical simulations of surface relaxation for perovskite titanates. *Surf. Sci.* **2000**, *462*, 19–35. [CrossRef]
109. Heifets, E.; Eglitis, R.I.; Kotomin, E.A.; Maier, J.; Borstel, G. *Ab initio* modeling of surface structure for $SrTiO_3$ perovskite crystals. *Phys. Rev. B* **2001**, *64*, 235417. [CrossRef]
110. Ho, J.; Heifets, E.; Merinov, B. *Ab initio* simulation of the $BaZrO_3$ (001) surface structure. *Surf. Sci.* **2007**, *601*, 490–497. [CrossRef]
111. Heifets, E.; Dorfman, S.; Fuks, D.; Kotomin, E.; Gordon, A. Atomistic simulation of surface relaxation. *J. Phys. Condens. Matter* **1998**, *10*, L347. [CrossRef]
112. Pilania, G.; Ramprasad, R. Adsorption of atomic oxygen on cubic $PbTiO_3$ and $LaMnO_3$ (001) surfaces. A density functional theory study. *Surf. Sci.* **2010**, *604*, 1889–1893. [CrossRef]
113. Fechner, M.; Ostanin, S.; Mertig, I. Effect of the surface polarization in polar perovskites studied from first principles. *Phys. Rev. B* **2008**, *77*, 094112. [CrossRef]
114. Zhuang, H.L.; Ganesh, P.; Cooper, V.R.; Xu, H.; Kent, P.R.C. Understanding the interactions between oxygen vacancies at $SrTiO_3$ (001) surfaces. *Phys. Rev. B* **2014**, *90*, 064106. [CrossRef]
115. Piskunov, S.; Heifets, E.; Eglitis, R.I.; Borstel, G. Bulk properties and electronic structure of $SrTiO_3$, $BaTiO_3$, $PbTiO_3$ perovskites: An *ab initio* HF/DFT study. *Comput. Mater. Sci.* **2004**, *29*, 165–178. [CrossRef]
116. Hay, P.J.; Wadt, W.R. *Ab initio* effective core potentials for molecular calculations. Potentials for K to Au including the outermost core orbitals. *J. Chem. Phys.* **1984**, *82*, 299–310. [CrossRef]
117. Mayer, I. Bond Order and Valence: Relations to Mulliken's Population Analysis. *Int. J. Quantum Chem.* **1984**, *26*, 151–154. [CrossRef]
118. Bochicchio, R.C.; Reale, H.F. On the nature of crystalline bonding: Extension of statistical population analysis to two- and three-dimensional crystalline systems. *J. Phys. B* **1993**, *26*, 4871–4883. [CrossRef]
119. Shi, H.; Chang, L.; Jia, R.; Eglitis, R.I. *Ab initio* calculations of the transfer and aggregation of *F* centers in CaF_2. *J. Phys. Chem. C* **2012**, *116*, 4832–4839. [CrossRef]
120. Mabud, S.A.; Glazer, A.M. Lattice parameters and birefringence in $PbTiO_3$ single crystals. *J. Appl. Cryst.* **1979**, *12*, 49–53. [CrossRef]
121. Edwards, J.W.; Speiser, R.; Johnston, H.L. Structure of Barium Titanate at Elevated Temperatures. *J. Am. Chem. Soc.* **1951**, *73*, 2934–2935. [CrossRef]
122. Okazaki, A.; Scheel, H.J.; Müller, K.A. The lattice constant vs. temperature relation around the 105 K transition of a flux-grown $SrTiO_3$ crystal. *Phase Trans.* **1985**, *5*, 207–218.
123. Aoyagi, S.; Kuroiwa, Y.; Sawada, A.; Tanaka, H.; Nishibori, E.; Takata, M.; Sakata, M. Direct observation of covalency between O and disordered Pb in cubic $PbZrO_3$. *J. Phys. Soc. Jpn.* **2002**, *71*, 2353–2356. [CrossRef]
124. Benthem, K.; Elsässer, C.; French, R.H. Bulk electronic structure of $SrTiO_3$: Experiment and theory. *J. Appl. Phys.* **2001**, *90*, 6156–6164. [CrossRef]
125. Wemple, S.H. Polarization Fluctuations and the Optical-Absorption Edge in $BaTiO_3$. *Phys. Rev. B* **1970**, *2*, 2679–2689. [CrossRef]
126. Robertson, J. Band offsets of wide-band-gap oxides and implications for future electronic devices. *J. Vacuum. Sci. Technol. B* **2000**, *18*, 1785–1791. [CrossRef]
127. Eglitis, R.I.; Popov, A.I. Systematic trends in (001) surface *ab initio* calculations of ABO_3 perovskites. *J. Saudi Chem. Soc.* **2018**, *22*, 459–468. [CrossRef]
128. Eglitis, R.I. Comparative First-Principles Calculations of $SrTiO_3$, $BaTiO_3$, $PbTiO_3$ and $CaTiO_3$ (001), (011) and (111) Surfaces. *Ferroelectrics* **2015**, *483*, 53–67. [CrossRef]
129. Eglitis, R.I.; Vanderbilt, D. First-principles calculations of atomic and electronic structure of $SrTiO_3$ (001) and (011) surfaces. *Phys. Rev. B* **2008**, *77*, 195408. [CrossRef]

130. Eglitis, R.I.; Rohlfing, M. First-principles calculations of the atomic and electronic structure of $SrZrO_3$ and $PbZrO_3$ (001) and (011) surfaces. *J. Phys. Condens. Matter* **2010**, *22*, 415901.
131. Wang, Y.X.; Arai, M. First-principles study of the (001) surface of cubic $SrZrO_3$. *Surf. Sci.* **2007**, *601*, 4092–4096. [CrossRef]
132. Bickel, N.; Schmidt, G.; Heinz, K.; Müller, K. Ferroelectric relaxation of the $SrTiO_3$ (100) surface. *Phys. Rev. Lett.* **1993**, *62*, 2009–2012. [CrossRef]
133. Hikita, T.; Hanada, T.; Kudo, M.; Kawai, M. Structure and electronic state of the TiO_2 and SrO terminated $SrTiO_3$ (100) surfaces. *Surf. Sci.* **1993**, *287*, 377–381. [CrossRef]
134. Piskunov, S.; Kotomin, E.A.; Heifets, E.; Maier, J.; Eglitis, R.I.; Borstel, G. Hybrid DFT calculations of the atomic and electronic structure for ABO_3 perovskite (001) surfaces. *Surf. Sci.* **2005**, *575*, 75–88. [CrossRef]
135. Eglitis, R.I. *Ab initio* calculations of $CaZrO_3$, $BaZrO_3$, $PbTiO_3$ and $SrTiO_3$ (001), (011) and (111) surfaces as well as their (001) interfaces. *Integr. Ferroelectr.* **2019**, *196*, 7–15. [CrossRef]
136. Slassi, A.; Hammi, M.; Rhazouani, O.E. Surface Relaxations, Surface Energies and Electronic Structures of $BaSnO_3$ (001) Surfaces: *Ab initio* Calculations. *J. Electron. Mater.* **2017**, *46*, 4133–4139. [CrossRef]
137. Heifets, E.; Dorfman, S.; Fuks, D.; Kotomin, E. Atomistic simulation of the [001] surface structure in $BaTiO_3$. *Thin Solid Film.* **1997**, *296*, 76–78. [CrossRef]
138. Heifets, E.; Dorfman, S.; Fuks, D.; Kotomin, E.; Gordon, A. [001] Surface Structure in $SrTiO_3$—Atomistic Study. *Surf. Rev. Lett.* **1998**, *5*, 341–345. [CrossRef]
139. Sorokine, A.; Bocharov, D.; Piskunov, S.; Kashcheyevs, V. Electronic charge redistribution in $LaAlO_3$ (001) thin films deposited at $SrTiO_3$ substrate: First-principles analysis and the role of stoichiometry. *Phys. Rev. B* **2012**, *86*, 155410. [CrossRef]